



BABEȘ-BOLYAI UNIVERSITY
FACULTY OF PHYSICS
DOCTORAL SCHOOL OF PHYSICS



From classical noble metal nanoparticles
to controlled nanoplatforms
for ultrasensitive SERS biodetection

Thesis Summary

Scientific Advisor:

Prof. Dr. Leontin David

PhD student:

Ioana Andreea Brezeștean

Cluj-Napoca

2022

Table of contents

Introduction	3
Chapter I. The use of vibrational techniques in the detection of complex biomolecules, bacteria and their secretions	6
I.1 Spectroscopic study of exopolysaccharides as potential bioresources	6
I.2 FT-IR Study of Exopolysaccharides.....	9
Chapter II. SERS use of chemically reduced silver nanoparticles	12
II.1 Detection of inorganic species and salts in natural mineral waters by Raman spectroscopy ..	12
II.2 SERS analysis of mineral waters.....	14
II.3 Colloidal silver nanoparticles for the detection of aquatic microorganisms	15
II.3.1 Raman analysis of aquatic microorganism culture batch	16
II.3.2 SERS analysis of aquatic mycoorganisms in solution.....	18
II.3.3 Raman and SERS single cell analysis	19
II.3.4 SERRS detection of fucoxanthin: quantification of the carotenoid in living cells of the diatom <i>C. closterium</i>	22
Chapter III. Structured nanoplatfoms for efficient SERS detection.....	23
III.1 3D nanoplatfoms fabricated by nanolithography.....	23
III.2 Detection of cyanotoxin Nodularin.....	28
III.2.1. Raman analysis of cyanotoxin Nodularin by DCRD (Drop Coating Raman Deposition)	29
III.2.2 SERS detection of cyanotoxin Nodularin	31
III.3 Self-assembled colloidal silver nanoparticles on solid substrates.....	33
III.3.1 SERS detection of thiabendazole fungicide	35
III.3.2 SERS detection of endosulfan insecticide.....	37
Final conclusions	41
References:	43
Appendix 1. Results and dissemination.....	52

Keywords: Raman, SERS, silver thin films, marine toxins, aquatic microorganisms, periodically ordered nanostructures, pesticides

Introduction

Vibrational spectroscopy methods have attracted considerable interest in various fields of research such as medicine, pharmaceuticals, environmental sciences and even the food industry due to their many advantages over conventional methods. Raman spectroscopy together with the latest technological devices is one of the most useful tools for obtaining specific information on the structure and properties of biomolecular compounds such as carotenoids, cyanotoxins, toxins or environmental pollutants.

In this scientific context, the present PhD thesis aims to address various methods for the synthesis of both colloidal suspensions (AgNPs) and Silver (Ag) in the form of thin films deposited on periodically ordered surfaces. SERS applications developed with these substrates have been used for the detection of various molecules ranging from cyanobacteria detected in waters, to diatoms, to the detection of cyanotoxins and pesticides.

In this PhD work, we have exploited the advantages of ultrasensitive spectroscopic methods starting from Raman techniques to **surface-enhanced Raman spectroscopy (SERS)** to detect and identify cyanobacteria, cyanotoxins and pesticides using AgNPs and developed new SERS substrates that are accessible, cheap and easy to implement in applications of interest such as environmental protection.

In order to have an overview of the theoretical considerations of the Raman effect and complementary techniques already known and well described, in the literature, **Chapter I** presents and discusses classical and quantum Raman theory together with its evolution. SERS is introduced and types of substrates in SERS applications are presented.

Chapter II presents the use of Raman spectroscopy and Fourier transform infrared spectroscopy (FT-IR) in real-time monitoring of purified exopolysaccharide (EPS) components from *Arthrospira platensis* (also known as *Spirulina sp.*). Preliminary spectra for EPS compared to the dextran molecule have been reported. We comprehensively assigned the recorded and observed Raman and IR bands for EPS extracted from *A. platensis*. We corroborated the experimental results with recent studies reporting similar saccharide species using Raman spectroscopy.

Chapter III presents the use of the SERS technique for the detection of inorganic salts in spring mineral waters, which were evaluated using AgNPs and their aggregation as a function of time in the first part. In the second part of the chapter, studies on the interface between AgNPs and lightly silicified *Cylindrotheca closterium* diatoms *in vivo*, both in cell culture and at the

single cell level, are presented. Polyunsaturated fatty acids were detected together with SERS markers specific to carotenoids and chlorophylls. Resonance Raman resonance (RR) and surface-enhanced resonance Raman scattering (SERRS) spectra of fucoxanthin were investigated in a concentration-dependent manner to prospect the capability of quantitative carotenoid estimation techniques in the live diatom species, *C. closterium*.

Chapter IV presents patterned nanoplatforms for SERS detection of molecules of interest in the environment. In the first part, 3D nanoplatforms fabricated by nanolithography are presented, the study also aims to develop substrates with great potential as SERS detection platforms. These were fabricated by nanoimprint lithography (NIL) in plastic and were coated with Ag films of 10-100 nm thickness by direct current (DC) deposition. The contribution of plasmonic nanostructures contained in the Ag films to the SERS amplification factor was evaluated.

The second part presents the characterization of the Nodularin (NOD) molecule from a vibrational point of view. In addition, NOD was detected by SERS at ultra-low concentrations using AgNPs, commercial nanopatterned substrates with inverted periodic pyramids (Klarite substrate), hydrophobic SpecTrimTM slides and nanolines fabricated in house. The detection limit reached for NOD detection using AgNPs was 58 pM in ethanol (EtOH) solution.

The last part of this chapter presents films fabricated by the convective self-assembly (CSA) technique from AgNPs on solid planar substrate and their use for SERS analysis of two types of pesticides, thiabendazole (TBZ) and α -endosulfan (α -ES). These AgNPs films are used as such or hydrophobised using octanethiol and hexanethiol for better anchoring of ES near the metal surface. SERS measurements of TBZ and ES are explored and analyzed in correlation with density functional theory (DFT) calculations. The present study demonstrates the utility of self-assembled films of colloidal nanoparticles as SERS substrates and contributes to the development of efficient SERS sensors for the specific detection and identification of pesticides.

The most common currently active SERS substrates can be classified into the following three generic categories: (1) metal nanoparticles in suspension; (2) self-assembled metal nanoparticles on solid substrates; and (3) nanostructures fabricated on solid substrates by nanolithography.

In order to achieve maximum Raman signal amplification, the wavelength of the incident radiation must be matched to the substrate metal. Thus, for silver the 488 and 514.5 nm excitation lines of the argon ion laser are used.

Metallic colloids are widely used as active media because of the ease with which they are prepared. Colloids used as SERS substrates are very attractive because they can be prepared in a reproducible way with minimal cost and commercial availability. The most commonly used colloids are based on silver or gold nanoparticles in the 10 - 150 nm range. There are several suggested methods for preparing silver colloids and these are based on the chemical reduction of Ag ions to Ag⁰. The two most common methods suggested are Lee-Meisel¹ and Leopold². These produce small (25-50 nm) monodisperse colloidal particles needed to avoid self-aggregation and further increase SERS amplification. The sizes of nanoparticles in colloidal suspension can be determined either using a scanning electron microscopy (SEM) technique or UV-Vis measurements. Such colloids can be dried or deposited on various substrates to fabricate planar metal nanostructures.

Other active SERS substrates are nanoparticle deposition films, which offer high reproducibility of results, commercial SERS surfaces such as Klarite^{3, 4}, Tienta SpectRIM⁵ or SERSitive⁶ or ordered, simple or functionalized nanostructured surfaces. The characteristics of a high-performance active SERS substrate are :

- High interaction surface given by the roughness of the substrate which provides good electromagnetic field amplification as well as reproducibility and stability.
- SERS performance controlled by fabricating periodic patterning or nanostructures with certain optical properties, specific to the targeted application.
- Possibility to perform quantitative SERS measurements if a standard is used to monitor any changes due to substrate changes⁷.

Current major challenges in SERS spectroscopy

The major challenges and limitations of the current known SERS technique are: (1) this method requires contact between the proposed enhancement surface and the analyte being used (2) substrates degrade over time, leading to a decrease in signal; (3) limited selectivity of substrates for a given analyte; (4) limited substrate reuse; and (5) issues related to homogeneity and reproducibility of the SERS signal⁸. The sometimes poor reproducibility of the SERS signal is a major challenge that is due to a number of factors in practical applications.

Chapter I. The use of vibrational techniques in the detection of complex biomolecules, bacteria and their secretions

I.1 Spectroscopic study of exopolysaccharides as potential bioresources

Bacterial exopolysaccharides (EPS) are biopolymers secreted during biofilm formation and contain a variety of sugar components, from neutral sugars (e.g. rhamnose) to monomers such as glucose, galactose and mannose, as well as amino sugars (N-acetylamino sugars). These biopolymers have been extensively and systematically researched for decades in search of new industrial resources, new anticancer drugs, pharmaceuticals, immunomodulatory or health beneficial products with minimal production costs⁹⁻¹³. Despite all these efforts, only a few bacterial EPS are exploited for their commercial value, such as bacterial cellulose, alginate, dextran, xanthan gum, etc.⁹. The natural variability of these by-products determines their properties defined by their chemical composition, molecular structure, average molecular weight, glycosyl, linkages and configurations.

In this context, this subchapter aims to implement Raman and FTIR spectroscopies to clarify some aspects on the unique properties of cyanobacterial (*A. platensis*) EPS. EPS have a high potential as exploitable bioresources, after purification, in food, cosmetic and pharmaceutical production processes. Just a few examples of their further use would be: low calorie food additives, superior bioactive and therapeutic blood plasma substitutes compared to dextran-based plasma, improved drug delivery control.

There are two recognised types of EPS: EPS 'released' into the growth medium and EPS bound to the surface of the body, 'capsular polysaccharides'. The aim of this study is to identify the major components of EPS released by *A. platensis* species. We used a stepwise purification of EPS based on the findings of Xu *et al.*¹⁴. Their study shows how variation in the concentration of ethanol used to purify natural EPS influences the precipitation of polysaccharides of different molecular sizes and structures. This suggests that in the case of natural EPS extraction by ethanol precipitation, the ethanol concentration needs to be optimized for each type of sample.

During mature biofilm development, the matrix containing extracellular polymeric substances forms a complex 3D architecture consisting of polysaccharides, proteins, lipids, nucleic acids, etc. EPS production is usually associated with growth or induced stressors. Using Raman microspectroscopy, biofilms can be investigated non-invasively even in growth medium

¹⁵. There are few studies performed to characterize spectral variations for purified EPS in a stepwise manner. In this case, we separated EPSs released into the growth medium from cyanobacterial biomass and purified them.

Raman investigation is usually based on associating the intensity or wavenumbers of Raman bands with the specific molecular structure of the samples and their concentration. In this case, we expect to find similar fingerprints attributed to monosaccharide species that are found in different proportions as they compose heteropolysaccharides (HePS - a complex of 5 to ⁹ monomers with similar structural elements). This is supported by the strong Raman bands observed around 1062 cm⁻¹ in addition to bands specific to dextran, a common homopolysaccharide (HoP). HePS are composed of repeating monosaccharide subunits such as d- α -glucose, d-galactose, l-rhamnose or other derivatives such as N-acetylglucosamine or N-acetylgalactosamine ¹³ (**Figure 1.1**).

Several standard saccharide species other than dextran, which should be found in the EPS samples analysed, were investigated by Raman spectroscopy and are shown as reference spectra (**Figure 1.2** and **Figure 1.3**). Since the Raman signal has spectral features that are mediated from all saccharide-like components, we chose to look for significant spectral variations in the Raman bands (intensity, position) assigned to these particular components. Raman spectroscopy is a promising method for real-time identification and monitoring of living cells and allows accurate high-throughput screening ^{15,16} (directly in Petri dishes containing viable cultures). The reported Raman detection limit for EPS extracted from algae was 100 mg/L ¹⁷.

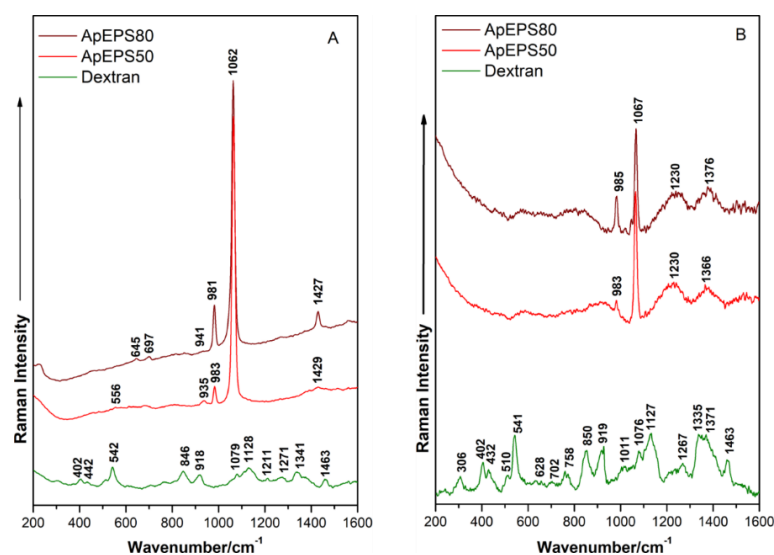


Figure 1.1 Raman spectra of dextran, ApEPS50 and ApEPS80, respectively, recorded with laser lines 532 nm (A) and 633 nm (B), respectively (Reproduced from I. Brezeştean, M. Bocăneală, A. M.R Gherman, S. Porav, I. Kacsó, E. Rakosy-Tican, N. E. Dina, doi.org/10.1016/j.molstruc.2021.131228, J. Mol. Struct) ¹⁸.

The Raman bands for saccharides are typically found in the region between 1000 - 1200 cm^{-1} and 1300 - 1500 cm^{-1} ¹⁹. In addition, very similar Raman fingerprints have been found for β -D-glucose and D-(+)-dextrose (α -D-glucose), as well as their dimers and polymers. The intense Raman band present at 1062/1067 cm^{-1} in the EPS and 1079 cm^{-1} spectra, respectively, but very weak for dextran, is attributed to the C - C stretching vibration in carbohydrates. Since the Raman fingerprint of dextran does not show this band with as high intensity, we tend to attribute the Raman band at 1062 cm^{-1} to other constituents in saccharide species (Raman spectral fingerprints shown in **Figures 1.2** and **1.3**).

The saccharides showing such strong Raman bands at this position are L(+)-ramnose, D(+)-mannose and glucose anomers, but reported as a strong band with two divisions ²⁰, and in D(+)-galactose as a very sharp band ²¹. Rhamnose is the only species also showing a medium intensity Raman band at 980 cm^{-1} , as found in the EPS spectral fingerprints reported here. The vibrational mode at 1127 cm^{-1} is present only in the spectra of dextran, and is commonly attributed to carbohydrates, but also to several groups of molecules such as proteins and lipids. The absence of proteins and lipids, however, is supported by the absence of specific Raman bands in the range 1600 - 1750 cm^{-1} .

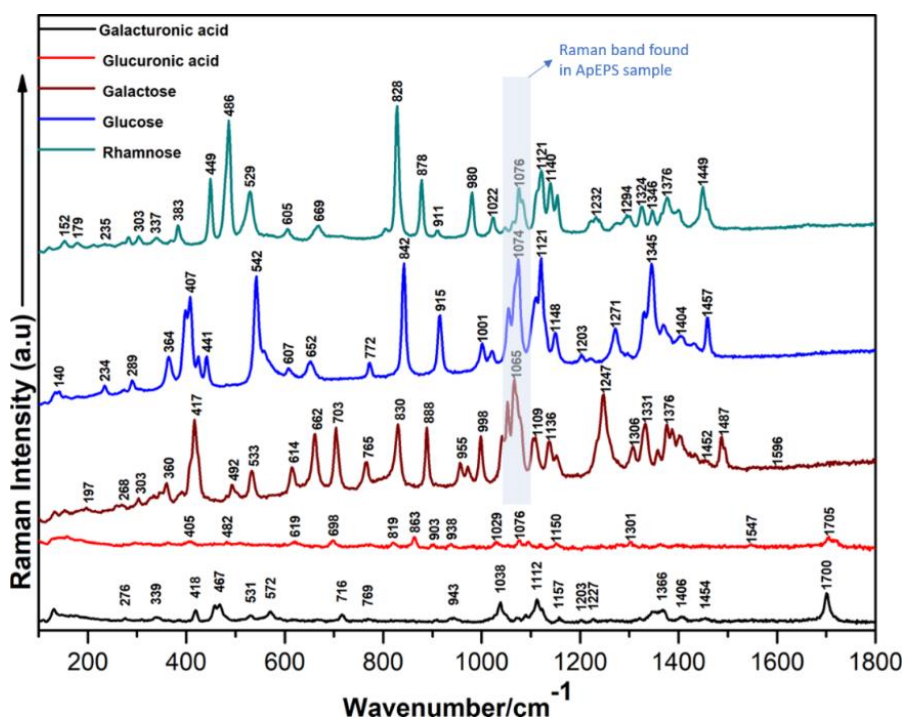


Figure 1.2 Raman spectra of some standard saccharides recorded with the line532 nm laser

(Reproduced from I.Brezeștean, M. Bocăneală, A. M.R Gherman, S. Porav, I. Kacsó, E. Rakosy-Tican, N. E.

Dina, doi.org/10.1016/j.molstruc.2021.131228, J. Mol. Struct) ¹⁸.

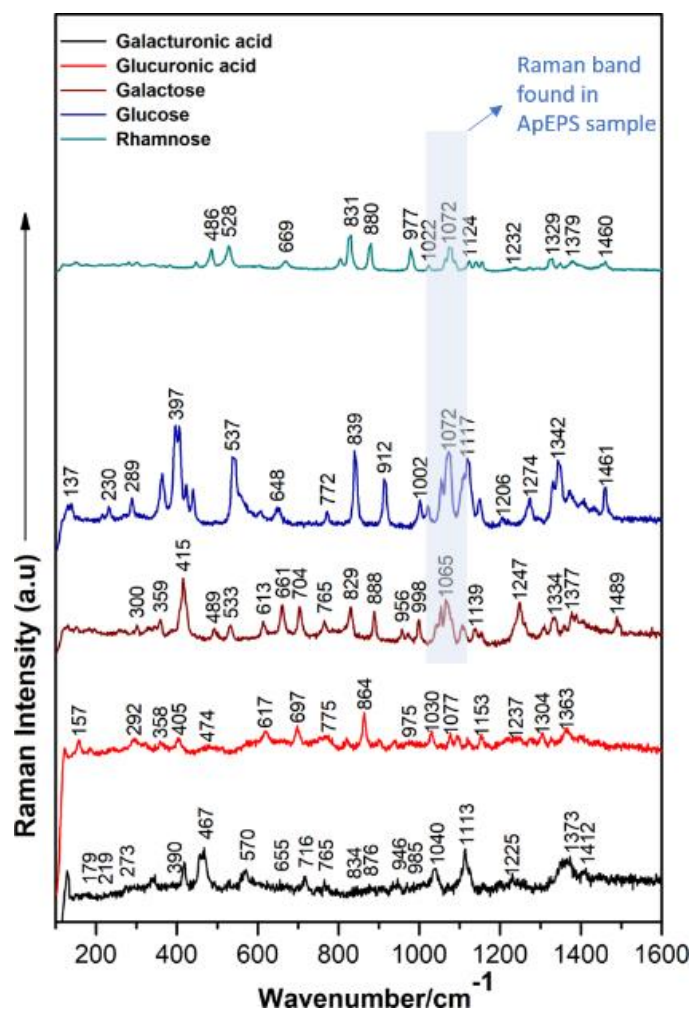


Figure 1.3 Raman spectra of some standard saccharides recorded with the 633 nm laser line (Reproduced from I. Brezeştean, M. Bocăneală, A. M.R Gherman, S. Porav, I. Kacsó, E. Rakosy-Tican, N. E. Dina, doi.org/10.1016/j.molstruc.2021.131228, J. Mol. Struct) ¹⁸.

1.2 FT-IR Study of Exopolysaccharides

As a complementary analysis, FTIR spectra were recorded and discussed as follows. The FTIR spectra of EPS samples, extracted with 96% ethanol (ice cold) at different concentrations, are shown in **Figures 1.4**.

By comparing the IR spectra of the two samples it was observed that the broad band with the maximum at 3455 cm^{-1} in the spectrum of ApEPS50 sample, attributed to the stretching vibration of -OH groups in polymeric compounds of polysaccharide nature ²²⁻²⁴, is shifted to 3463 cm^{-1} in the spectrum of ApEPS80 sample. The absorption bands at 2925 and 2854 cm^{-1} were attributed to the asymmetric and symmetric C - H stretching vibration of CH₂ and CH₃ groups ^{23,24}. The intensity of the broad vibrational band at 1689 cm^{-1} , attributed to the presence of C = O or C = C groups in the analysed structures ²³, is higher in the spectrum of the ApEPS80

sample. The absence of a strong band at 1647 cm^{-1} in the IR spectra, which would be attributed to $\text{C} = \text{O}$ or $\text{C} = \text{N}$ bonds in amide I²⁴, indicates that there is no protein in the EPS samples, which is consistent with the Raman determinations performed. The intense band at 1447 cm^{-1} , attributed to $\text{C} - \text{O}$ and CH_2 ^{24,25} stretching vibrations, shifts to 1461 cm^{-1} with lower intensity for the ApEPS80 sample.

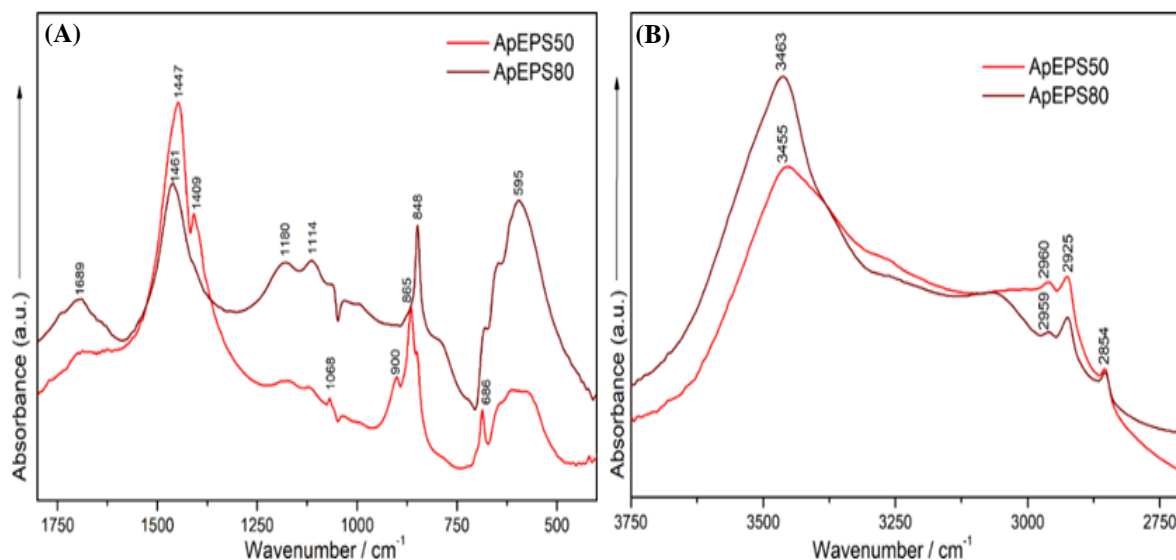


Figure 1.4 (A) FTIR spectra of ApEPS samples, spectral range $1800\text{-}400\text{ cm}^{-1}$. (B) FTIR spectra of ApEPS samples, spectral range $3750\text{-}2700\text{ cm}^{-1}$ (Reproduced from I. Brezeştean et al. doi.org/10.1016/j.molstruc.2021.131228, J. Mol. Struct) ¹⁸.

In the spectral range $1000 - 1200\text{ cm}^{-1}$, stretching vibrations of $\text{C} - \text{OH}$ side groups and $\text{C} - \text{O} - \text{C}$ glycosidic bonds, attributed to polysaccharides and polysaccharide-type structures, are present. The faint absorption bands at 1123 and 1068 cm^{-1} observed in the spectrum of ApEPS50 can be attributed to the stretching vibrations of the pyranoserings, and they appear with inverted intensity and offset at 1114 and 1062 cm^{-1} , respectively, in the spectrum of ApEPS80. The presence of strong absorption bands in the range $600 - 950\text{ cm}^{-1}$ indicates glycosidic binding of polysaccharides²².

Regarding the intensity ratios for the first two bands, the most intense in the Raman spectra of the ApEPS samples, we observed a particular trend that is also seen in the FT-IR spectra. The Raman bands at 958 cm^{-1} (laser line - 633 nm) and 981 cm^{-1} (laser line - 532 nm) show a 2-fold increase in intensity ($1:0.39$ for 532 and $1:0.52$ for 633 nm). The intensity ratio of the $1067/1062\text{ cm}^{-1}$ Raman band follows an opposite trend - it decreases in intensity from the first purification step (ApEPS50) to the second step (ApEPS80), but the ratio is not so

significant (1:1.06 for 532 and 1:1.25 for 633 nm). Thus, the most intense Raman band observed is slightly influenced by the excitation laser line during the purification process.

Consequently, the attribution of this band to a phosphonate-type by-product is better supported by the results. Similar extracellular organic species were reported by Stuart *et. al*²⁶ when they followed isotopically labeled EPS that were reused by cyanobacterial cells. The concentration of ethanol used for purification is also known to influence precipitated saccharide species in the extracellular matrix, but in this case, for the major constituent of the purified samples (ApEPS50 and ApEPS80), the concentration of ethanol does not significantly alter the spectral response. We assume that in the purified samples we can still find in high proportion some phosphonate species as organic salts released from the biomass. Therefore, more effort should be made to make the purification protocol more efficient. For this, we intend to apply dialysis membrane purification and subsequent lyophilization. Additional molecular insight was found in the ¹³C CP-MAS spectra. It is dominated by NMR lines at 172.4 and 167.9 ppm, which can be best attributed to ¹³C found in different carbonate systems²⁷.

Two much smaller lines, with amplitudes less than 1% of the dominant resonances, are identified at 73.3 and 64 ppm - marked with red arrows in the image. Their positions are characteristic of different carbon sites in glucose, indicating the presence of a minute amount of saccharides. The limited sensitivity for non-analytical purity samples and the specificity of the NMR technique for species containing organic matter (with C in the composition) explain these results. We conclude that carbonate species are mainly detected in our samples using NMR, while saccharide species and other organic impurities were revealed by vibrational spectra in higher contributions.

By corroborating the recorded spectral results with recent studies reporting similar saccharide species, we were able to accurately assign the recorded Raman bands. The complexity of deciphering information from the vibrational spectra reported in the present study lies in the number of monosaccharides and/or their derivatives that are combined in the final biosynthesized polymer structure. We reported the Raman and FT-IR fingerprints assigned to the monosaccharide species found in different proportions as composing HePS, as well as other impurities due to the fact that, in addition to the Raman bands characteristic of saccharides, we could observe specific bands assigned to phosphates. The saccharide species tentatively identified in our samples are rhamnose, D(+)-glucose and D(+)-galactose.

Chapter II. SERS use of chemically reduced silver nanoparticles

In the following we exploited Ag colloids prepared by both citrate and hydroxylamine reduction methods to detect salts specific to natural mineral waters of interest and diatoms specific to natural seawater, respectively.

II.1 Detection of inorganic species and salts in natural mineral waters by Raman spectroscopy

The raw characteristic FT-Raman spectra (0 - 3600 cm^{-1}) of the four mineral spring water samples (Lucius, Emerita, Carola and Bonifacius) are shown in **Figure 2.1**. The FT-Raman spectra of the water samples show characteristic bands of bicarbonate, carbonate and sulphate anions as well as free carbon dioxide and trace organics in aqueous solution. The assignment of these bands is in good agreement with published data for similar species in natural fluid inclusions (paleofluids), seawater, mineral water²⁸ or synthetic aqueous solutions^{29,30-33}.

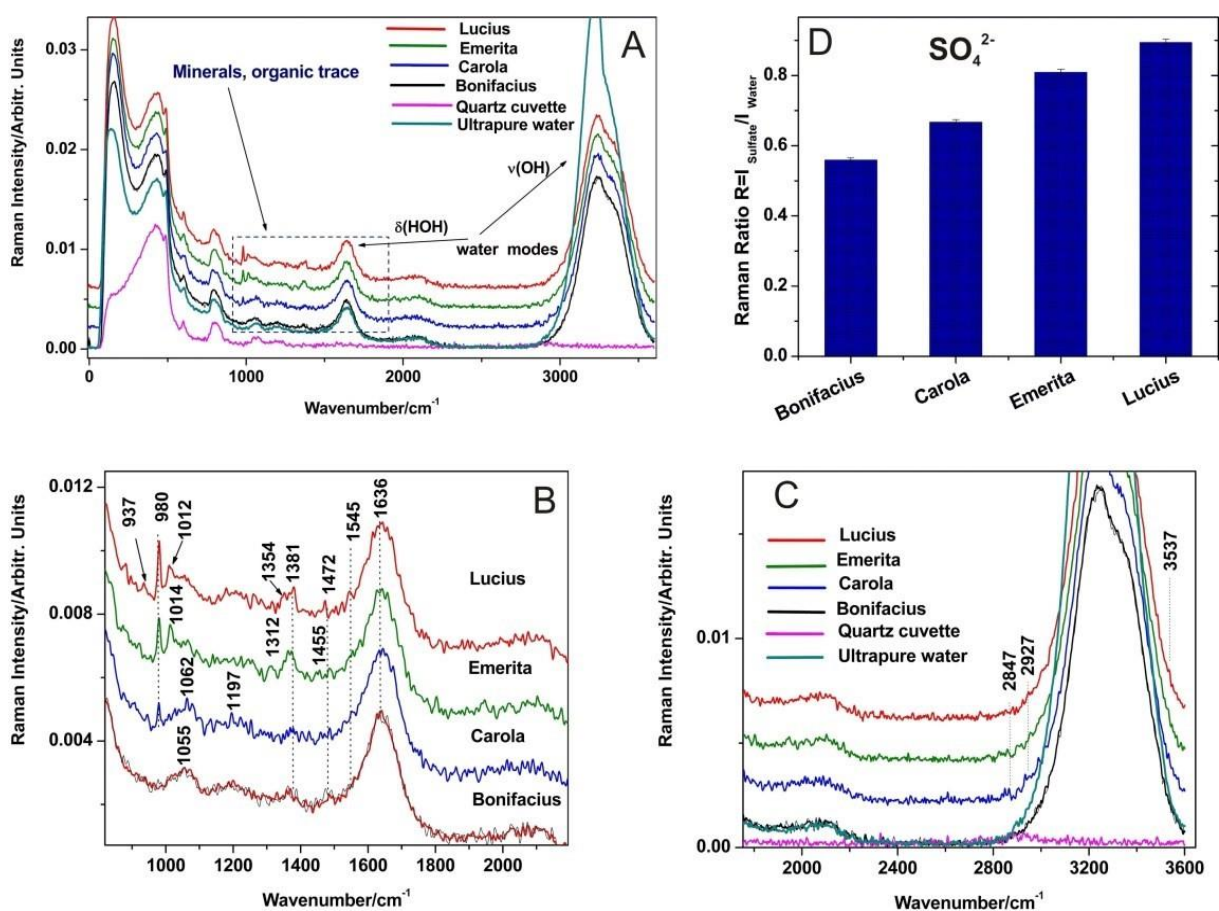


Figure 2.1. (A) FT-Raman spectra of natural mineral waters: Lucius, Emerita, Carola and Bonifacius (0 - 3600 cm^{-1}); (B) Zoom of A. (C) Zoom of high wavenumber range in A; organic trace bands are highlighted.

Excitation: 1064 nm, 350 mW. (D) Plot of the ratio of the surface area of the sulphate bands at 980 cm^{-1} to water for the four samples. (Reproduced from S. Cîntă Pinzaru, M. Ardeleanu, I. Brezeştean, F. Nekvapil, M.M. Venţer; 11: 800 - 812. DOI: 10.1039/c8ay02580k, *Anal. Methods*)³⁴.

A similar hierarchy of springs in terms of $(\text{SO}_4)_2^-$ content, but with a different growth factor, emerges from the analytical data (1997) displayed at the mouths of springs for public information purposes, with 1.570 g/L for Lucius, 1.381 g/L for Emerita, 0.211 g/L for Carola and 0.165 g/L for Bonifacius, respectively. The calculation of $1.570/1.381 = 1.13$ for the Lucius/Emerita sulphate concentration ratio translates to a 1.26-fold increase in the Raman data.

In addition to bands assigned to vibrational modes of inorganic anions, FT-Raman spectra of all water samples reveal several weak bands in the high wavenumber range (1455, 1472, 1545, 2847, 2927 cm^{-1}), suggesting organic contributions to the overall Raman signal. For example, CH bending modes can be assigned in the low wavenumber range, while stretching modes can be assigned in the high wavenumber range for a wide variety of organic compounds³⁵. FT-Raman spectra of powdered salt samples (0 - 3600 cm^{-1}) and details of the spectral range 750 - 1500 cm^{-1} are shown in **Figure 2.2A** and **2.2B** respectively. Reference FT-Raman spectra of pure anhydrous and hydrated polycrystalline sodium sulfate, as well as calcium carbonate and calcite mineral are shown in **Figure 2.2C** for comparison.

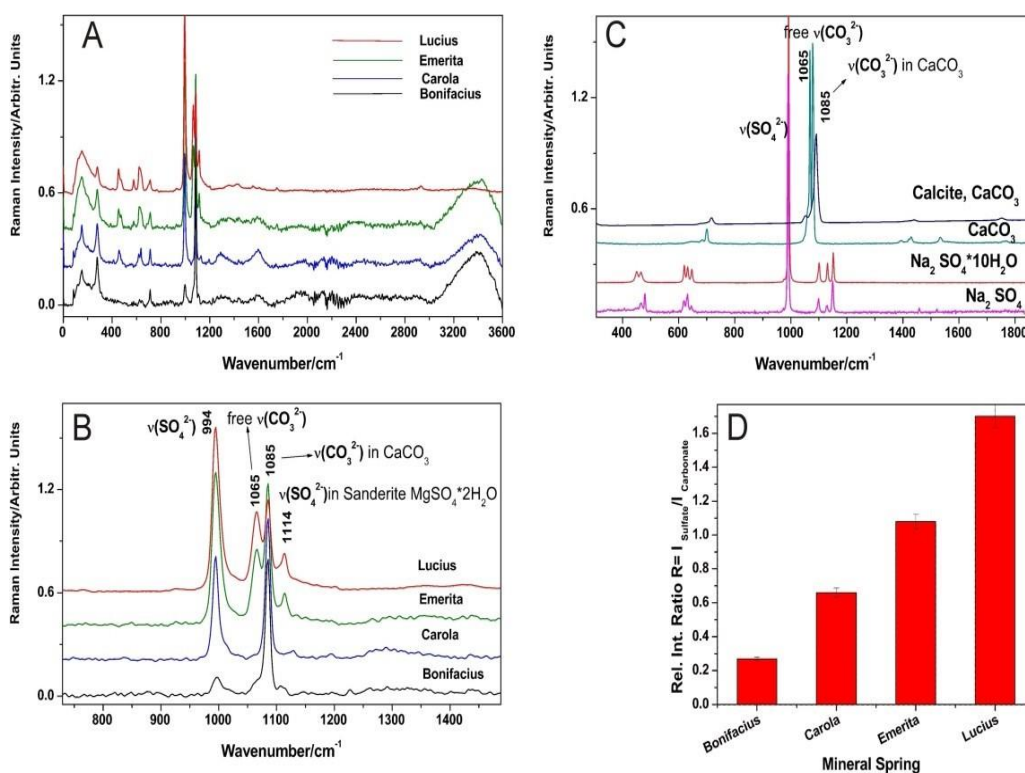


Figure 2.2 (A) FT-Raman spectra of salt samples from natural mineral waters: Lucius, Emerita, Carola and Bonifacius (0-3600 cm^{-1}). (B) Zoom of the range 750-1500 cm^{-1} in A. (C) FT-Raman spectra of anhydrous and

hydrated polycrystalline sodium sulphate, calcium carbonate and mineral calcite ($400\text{-}1800\text{ cm}^{-1}$). (D)
 Graphical representation of the intensity of the sulphate band at 994 cm^{-1} relative to that of carbonate at 3.96 % of the data. (Reproduced from S. Cîntă Pinzaru, M. Ardeleanu, I. Brezeştean, F. Nekvapil, M.M. Venţer; 11: 800 - 812. DOI: 10.1039/c8ay02580k, Anal. Methods) ³⁴.

II.2 SERS analysis of mineral waters

SERS analyses of mineral waters (Lucius, Emerita, Carola and Bonifacius) are approached comparatively to prospect the ability of the technique to detect any organic components. During SERS sample preparation, a rapid change in nanoparticle colour was observed when mineral water droplets were added. Their anion-rich content was expected to ensure the aggregation of nanoparticles and therefore their optical extinction was investigated. (**Figure 2.3**). The extinction spectra of the raw mineral waters (**Figure 2.3A**) show barely visible absorption bands in the UV range (200 - 400 nm), which are due to organic traces. To determine the influence of the mineral content of the waters on AgNPs, extinction spectra of mineral water-AgNPs mixtures were recorded together with those of pure AgNPs (**Figure 2.3B**). Since the physical measurements were performed in absorption mode, the optical spectra in **Figure 2.3** are displayed as absorption versus wavelength. The addition of mineral water to the AgNPs resulted in a decrease in the intensity of the absorption band, while the position at 424 nm remains constant.

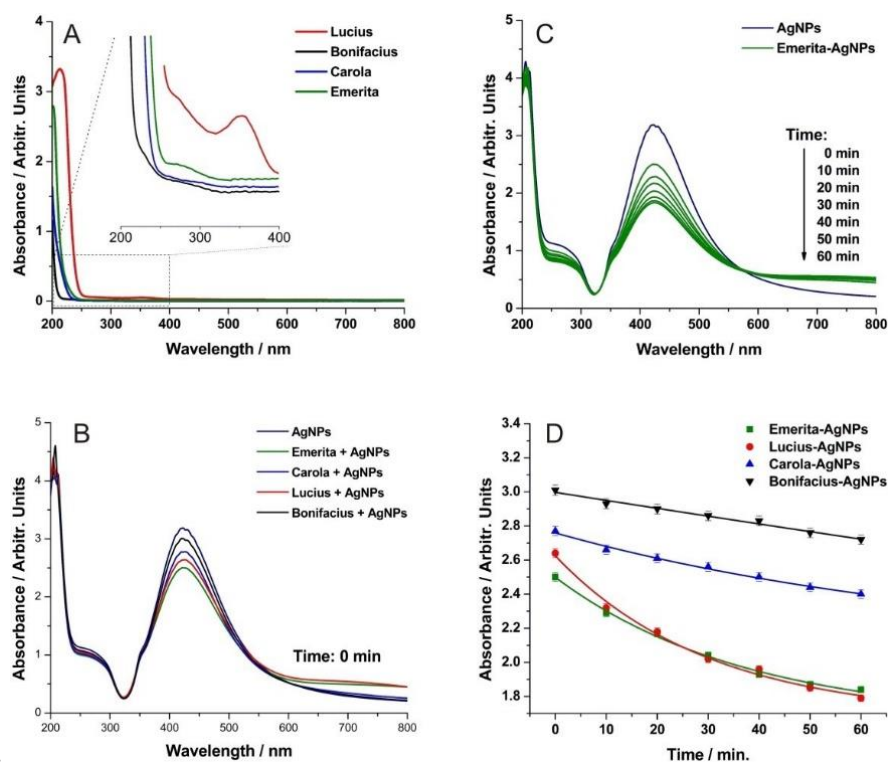


Figure 2.3 A) UV-Vis extinction spectra of natural mineral waters: Lucius, Emerita, Carola and Bonifacius (200-800 nm). (B) UV-Vis extinction spectra of AgNPs and mineral water-AgNPs mixtures, freshly prepared. (C)

UV-Vis extinction spectra as a function of time of the Emerita water-AgNPs mixture. (D) Graphical representation of the absorbance at 424 nm of the water-AgNPs mixtures as a function of time. (Reproduced from S. Cîntă Pinzaru, M. Ardeleanu, I. Brezeştean, F. Nekvapil, M.M. Venţer; 11: 800 - 812. DOI: 10.1039/c8ay02580k, Anal. Methods) ³⁴.

Raman spectra of the fine powder salts obtained as solid residues after water evaporation revealed predominantly carbonate (1085 cm^{-1} , 712 cm^{-1}), polymorphic calcite and sulphate (994 cm^{-1}) vibrational modes consistent with the presence of minerals resulting from dissolution of the underlying rocks. Rock layers comprising dolomite, serpentinite and other metamorphic rocks provide high mineralization.

SERS analyses of the waters were approached comparatively, revealed the ability of the technique to assess both organic and inorganic components, and thus is suitable for implementing sustainable management of carbonated spring waters. Mineral waters induced aggregation of AgNPs and provided a SERS fingerprint characteristic of beta-carotene. Extinction spectra of raw mineral waters and mineral waters and mineral water mixtures with AgNPs proved that the time-dependent aggregation was significantly related to the mineral content and thus water-specific.

II.3 Colloidal silver nanoparticles for the detection of aquatic microorganisms

The accumulation of mucilaginous cells and mucilaginous matter on a large scale, sometimes covering hundreds of square kilometres, could drastically hamper aquaculture activity, affect seawater quality, induce mortality of sedentary fauna, disrupt the plankton community and affect tourism activity. The slightly siliceous sheaths of *Cylindrotheca fusiformis* Reimann and Lewin, of diatom species has long been characterized ³⁶. Extensive studies ^{37,38} have been devoted to various compositional determinations in relation to growth conditions, as diatoms have shown great potential for biodiesel but also for aquaculture. In terms of chemical composition, cultured *C. closterium* showed palmitoleic acid (omega-7 monounsaturated fatty acid) as the dominant fatty acid, followed by oleic acid, while the most abundant saturated fatty acids were pentadecanoic acid and palmitic acid ³⁷. Other studies revealed differences in the chemical composition of *C. fusiformis* clones isolated and grown under batch conditions ³⁸.

To date, available studies on diatom composition are based on extraction and separation techniques. Extensive studies have focused on the sheath or frustule of different diatom species ^{36,39-41} using techniques such as SEM or AFM which have shown that each part of the silica

sheath is attached to organic material, while the whole body is surrounded by mucilaginous material. In addition, a first approach in understanding the uptake of AgNPs by *C. diatoms* using the AFM technique found that AgNPs enter the cell wall through the silicon valve region as NPs embedded in the organic matrix. AgNPs caused local damage inside the cell without destroying the cell membrane⁴⁰. In addition, secretion of extracellular polymeric material (EPM) was found to be stimulated by the presence of NPs and as a defence mechanism. The chemical composition of algal bodies and secreted substances usually requires separation and extraction techniques, with the main disadvantages of multi-step multi-processing and the required chemicals being relatively expensive and time-consuming.

In this study we investigated the interface between the living marine diatom *C. closterium* and AgNPs by exploiting the SERS technique both in cell culture and at the single cell level, in order to (i) relate both carotenoid content and mucilaginous secretion content to normal Raman and SERS signals, respectively, (ii) evaluate the spectral behaviour of diatoms in the presence of AgNPs in their native environment; (iii) assess the reproducibility of the results obtained with a compact and portable Raman equipment suitable for in situ monitoring of diatoms

II.3.1 Raman analysis of aquatic microorganism culture batch

To evaluate the Raman signal of the culture batch, we used both visible (532 nm) and near-infrared (1064 nm) excitation using a compact and portable Raman system. The Raman spectra of freshly collected algae from the diatom culture batch recorded with three different instruments are shown in **Figure 2.4 A**. The FT-Raman instrument with NIR excitation (1064 nm) provided a weak signal of the *Cylindrotheca* culture batch, almost similar to that of natural seawater collected from coastal water (southeast Adriatic coast in Dubrovnik). This is probably due to the longer acquisition time required, which could lead to a slow sedimentation of the cells on the bottom of the glass vial and consequently to a poor Raman scattering collected from the solution in the geometry of the FT-Raman instrument. The sulphate band at 978 cm⁻¹, typical of the FT-Raman spectrum of unprocessed seawater was the only major band in the culture solution (**Figure 2.4 A, c**), with the carotenoid signal barely exceeding the noise level for NIR excitation. The ratio of the relative Raman intensity of the sulphate stretching mode to the water stretching mode at 3214 cm⁻¹ ($R = \frac{1}{4} I(978)/I(3214)$) was calculated for both *Cylindrotheca* in the solution batch and unprocessed seawater. The Raman bands of diatom cells in solution observed for 532 nm excitation at 1528, 1156 and 1007 cm⁻¹ respectively along

with their linear and harmonic combinations in the range 2110 - 2700 cm^{-1} (**Figure 2.4 A**, spectrum **a**) are characteristic of carotenoids^{28,42-49}.

The spectral information provided by the portable equipment (**Figure 2.4 A**, spectrum **b**), although less sensitive, suggests the possibility of monitoring the status of the live cell culture and carotenoid content. The Raman band of *C. closterium* at 1528 cm^{-1} suggests that fucoxanthin is the most dominant species^{44,46,49}.

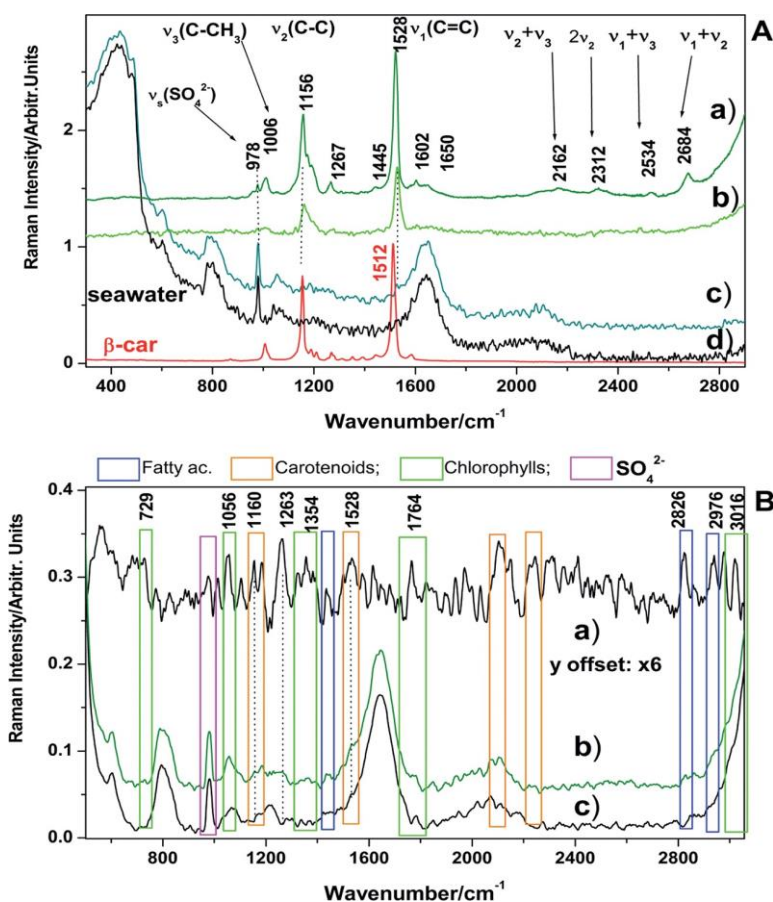


Figure 2.4 (A). Normalized Raman spectra of *C. closterium* culture solution recorded with a Renishaw instrument (a) with a compact, portable and fast DeltaNu spectrometer (b) and FT-Raman system (c), respectively. For comparison, FT-Raman spectra of raw seawater (d) and solid red *b*-carotene are shown). Excitation: 532 nm (a and b) and 1064 nm (c and d) (B). Spectral difference (a) between mean FT-Raman spectra of *Cylindrotheca* (b) and seawater (c). Although weak, the difference signal shows characteristic traces of chlorophylls, carotenoids, fatty acids and sulfate ions, which are highlighted in rectangles (Reproduced from S. Cîntă Pînzaru, C. Müller, S. Tomšić, M. M Vențer, I. Brezeștean, S. Ljubimir, B. Glamuzina, 42899-42910 DOI: 10.1039/C6RA4255D, RSC Advance)⁵⁰.

II.3.2 SERS analysis of aquatic mycoorganisms in solution

The SERS spectra of the diatom solution suspended on HY-AgNPs and LM-AgNPs are shown in **Figure 2.5 A** (range 300 - 1800 cm^{-1}).

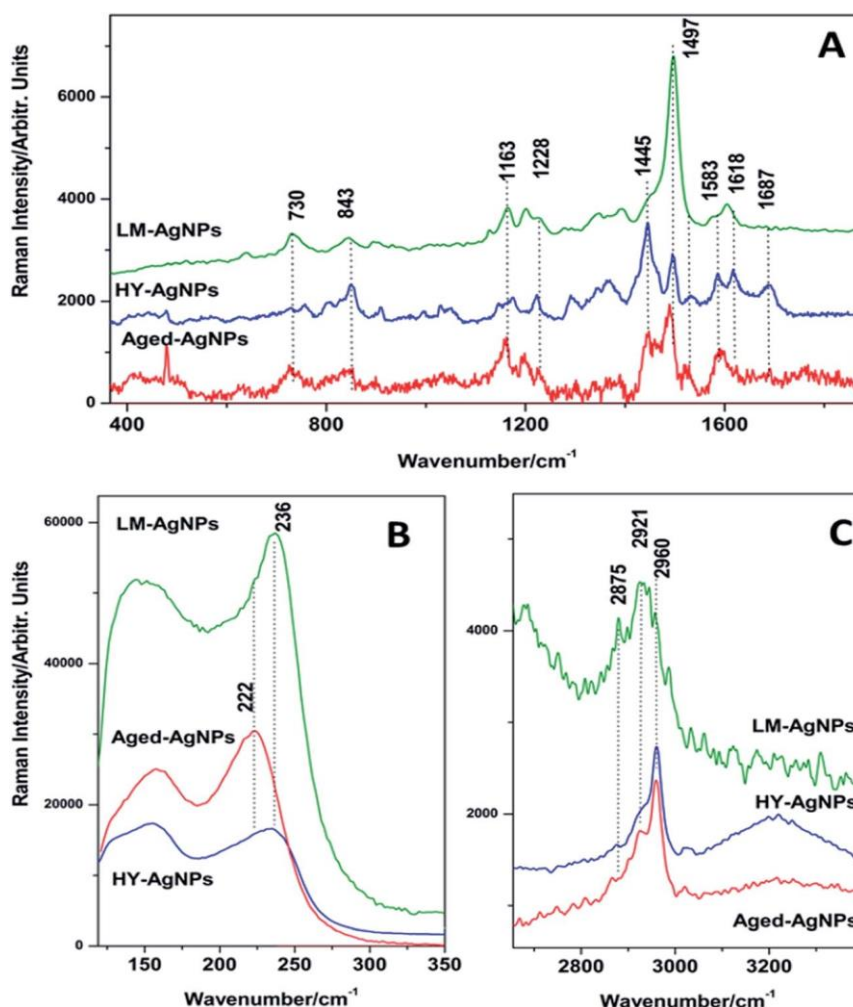


Figure 2.5 (A) SERS spectra of *Cyndrotheca* diatoms mixed with, *Lee-Meisel* (LM), reduced hydroxylamine (HY) and HY- old AgNPs, respectively. Details in the low (B) and high (C) wavenumber range are highlighted. Excitation: 532 nm (Reproduced from S. Cîntă Pînzaru, C. Müller, S. Tomšić, M. M Vențer, I. Brezeștean, S. Ljubimir, B. Glamuzina, 42899-42910 DOI: 10.1039/C6RA4255D, RSC Advance)⁵⁰

Figure 2.5 B and C highlights the range in the low (120 - 330 cm^{-1}) and high (2550 - 3200 cm^{-1}) wave region respectively. Adding a small amount of 10 μl of diatom culture to the batch of nanoparticles results in an instant colour change from dark yellow to dark blue-grey due to rapid aggregation in the presence of diatoms and anions in the batch culture, including seawater. Nanoparticle aggregation was confirmed by strong plasmon resonance shift of AgNPs and broadening of the absorption band across the visible range.

To date, this is the first SERS experiment performed on living diatoms, and little information on their molecules or in vivo behaviour is available. Nanoparticles are rapidly aggregated by salts in seawater and culture medium.

All three cases of SERS experiments showed an unexpected feature: the absence of the main Raman mode of diatoms characteristic of vibration at 1528 cm^{-1} . The presence of the SERS band at 1497 cm^{-1} could be attributed to the carotenoid adsorbed by AgNPs; however, a large shift of 31 cm^{-1} is quite unusual in SERS.

Such an interaction would require an instantaneous uptake of NPs through the diatom sheath and cell membrane, since the signal is observed within the first few seconds after SERS sample preparation. Most likely, fucoxanthin-chlorophyll proteins would be responsible for this SERS band, which is also dominant in aged AgNPs. This hypothesis is supported by the observation of other characteristic chlorophyll SERS bands at 730, 805, 910, 1165, 1228, 1346, 1369, 1618 and 1680 cm^{-1} , respectively.

Large differences between normal Raman and SERS signals (**Figure 2.4 A** and **2.5**) clearly indicate species other than carotenoids responsible for the diatom-AgNPs interaction. This result suggests that the (pre)resonance Raman effect observed in diatoms in culture solution is no longer dominant in SERS. Since the cell wall is a complex arrangement of siliceous and organic substances, comprising frustulins, pleuralins, silafins and long-chain polyamines^{40,51} AgNPs arriving in their vicinity could bind to their N-terminus, explaining the effect observed in SERS and due to Ag-N binding. The symmetric $\nu(\text{SiO})$ modes in the Raman spectra typically observed in siliceous materials at 787 and 764 cm^{-1} for silicic acid, respectively, would be present in the SERS signal along with typical Raman bands (430 , 800 , 1060 and 1200 cm^{-1} , respectively) attributed to the fundamental vibrations of the hydrated silicon glass framework. Very weak SERS signal at these positions was observed in the diatom spectra, indicating that the silicon material in frustule⁵¹ does not contribute substantially to the overall SERS signal.

II.3.3 Raman and SERS single cell analysis

The optical image provided by the Raman microscope for the $100\times$ objective (**Figure 2.6 inset**) shows the irradiated cells for Raman spectra acquisition. The raw Raman signal (**Figure 2.6 A, a** and **b**) recorded at the cell surface includes a strong fluorescence background and Raman bands of carotenoids. After background subtraction (**Figure 2.6 A, c** and **B, a-e**),

different cells showed the carotenoid-specific signal (fucoxanthin dominant). The dominant feature of the normal micro-Raman spectra collected from individual diatom cells was the C=C bond stretching mode of fucoxanthin at 1528 cm^{-1} whose intensity variation was observed from cell to cell and from different points on the green body of the same cell.

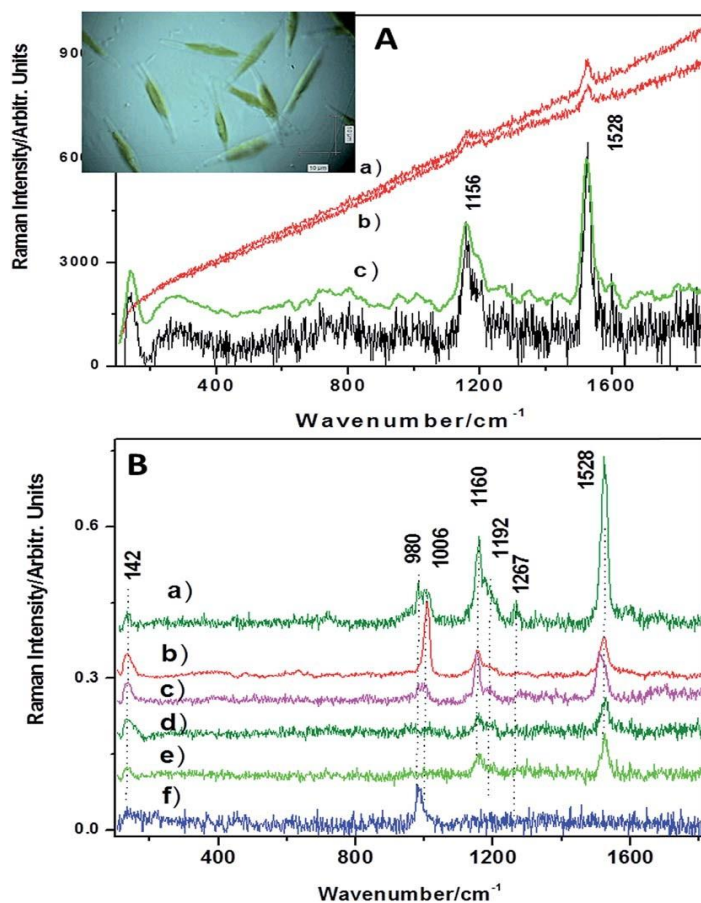


Figure 2.6 (A) Typical raw micro-Raman signal (a and b) of single *C. closterium* cells on a hydrophobic plate and background signal subtracted (c). The smooth signal is highlighted in green. Optical microscopy image of *C. closterium* cells coated with droplets on hydrophobic plate ($100\times$ objective) is shown in the inset. (B) Raman spectra collected from the green body of several live cells (a-e) and the transparent terminal body (f).

Excitation: 532 nm (Reproduced from S. Cîntă Pînzaru, C. Müller, S. Tomšić, M. M Vențer, I. Brezeștean, S. Ljubimir, B. Glamuzina, 42899-42910 DOI: 10.1039/C6RA4255D, RSC Advance)⁵⁰.

SERS spectra of individual diatoms are shown in **Figure 3.7** for both LM-AgNPs (**Figure 2.7 A**) and HY-AgNPs (**Figure 2.7 B**). The intense band at 236 cm^{-1} in **Figure 2.7 A** indicates a significant SERS chemisorption process of N-containing molecular species on the surface of NPs, as well as a different structure of the nanoaggregate network (band at 149 cm^{-1}), while the middle band at 222 cm^{-1} present in panel B suggests that the sample contains chemisorbed O species relative to HY-AgNPs^{52,53}.

In both cases, carotenoids were dominant, but with different results. The fucoxanthin band at 1528 cm^{-1} was absent in both cases. In the case of HY-AgNPs, the SERS signal collected from the diatom body (**Figure 2.7 B**, spectra *a-c*) clearly showed a strong contribution of β -carotene adsorbed by Ag, based on the similarity between band positions and relative intensities. When using LM-AgNPs nanoparticles, the SERS signal is dominated by conventional carotenoids with characteristic Raman bands (1156 , 1521 , 1526 cm^{-1} , respectively) and we do not have a feature of chemisorbed bands ²⁸. The additional bands observed at 1254 , 1359 , and 1690 cm^{-1} , respectively, were attributed to polyunsaturated fatty acids and chlorophylls ^{40,51,54–58}.

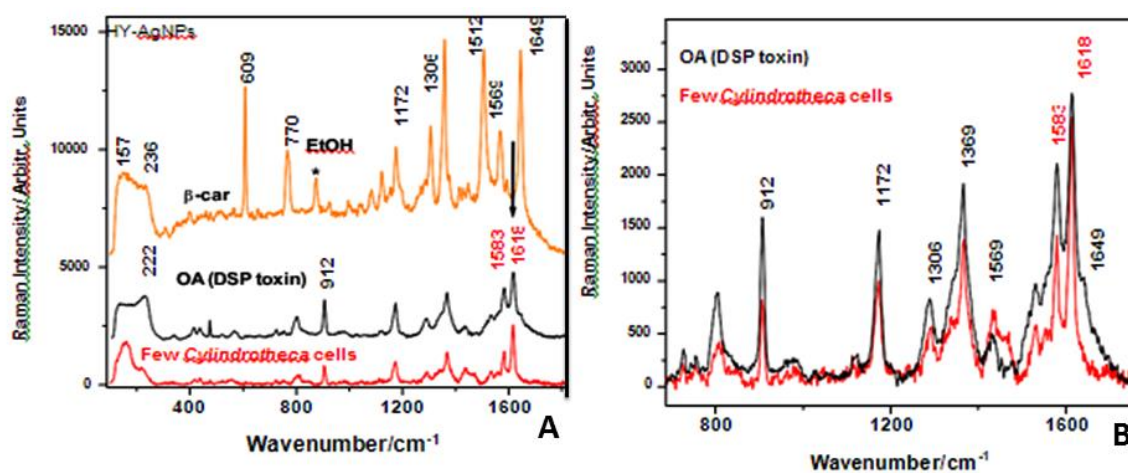


Figure 2.7 A: SERS spectra collected from *Cylindrotheca* diatom cells with HY-AgNPs compared to the SERS signal of a DSP toxin (okadaic acid). B: Detailed range $700\text{--}1800\text{ cm}^{-1}$ (Reproduced from S. Cîntă Pinzaru, C. Müller, S. Tomšić, M. M Vențer, I. Brezeștean, S. Ljubimir, B. Glamuzina, 42899-42910 DOI: 10.1039/C6RA4255D, RSC Advance) ⁵⁰.

In addition, the very strong SERS band at 225 cm^{-1} supports the hypothesis of O adsorption via carboxylic groups of fatty acids on the colloidal surface of Ag.

EPS represents a subtle network of cross-linked polysaccharide fibrils in fibril junctions and fibril-globular interconnections with globules connecting two or more fibrils ^{40,41}. The characteristic glucose units of polysaccharides exhibit Raman bands at 405 cm^{-1} (s), 440 cm^{-1} (m), 542 cm^{-1} (s), 650 cm^{-1} (mw), 772 cm^{-1} (mw), 841 cm^{-1} (ms), 914 cm^{-1} (ms), 1002 cm^{-1} (mw), 1022 cm^{-1} (m), 1054 cm^{-1} (m), 1075 cm^{-1} (ms), 1120 cm^{-1} (ms), 1149 cm^{-1} (m), 1272 cm^{-1} (m), 1296 cm^{-1} (ms), 1459 cm^{-1} (m) ^{18,59}.

II.3.4 SERRS detection of fucoxanthin: quantification of the carotenoid in living cells of the diatom *C. closterium*

To prospect for the detection of fucoxanthin Raman signal in native biological systems, Raman spectra were recorded from *C. closterium* cultures (**Figure 2.8**) isolated and cultured from fresh phytoplankton samples. Diatoms are rich in fucoxanthin⁶⁰⁻⁶⁴, however, they also contain other carotenoids that influence the spectral profile of the $\nu_1(\text{C}=\text{C})$ band. The spectral signal of *C. closterium* cells shows prominent main bands of carotenoids. The ν_1 , ν_2 and ν_3 bands were recorded at 1527, 1163 and 1015 cm^{-1} positions, respectively, slightly different from those in fucoxanthin solutions, which is characteristic for biological matrices (embedded in lipid membranes or protein carriers).

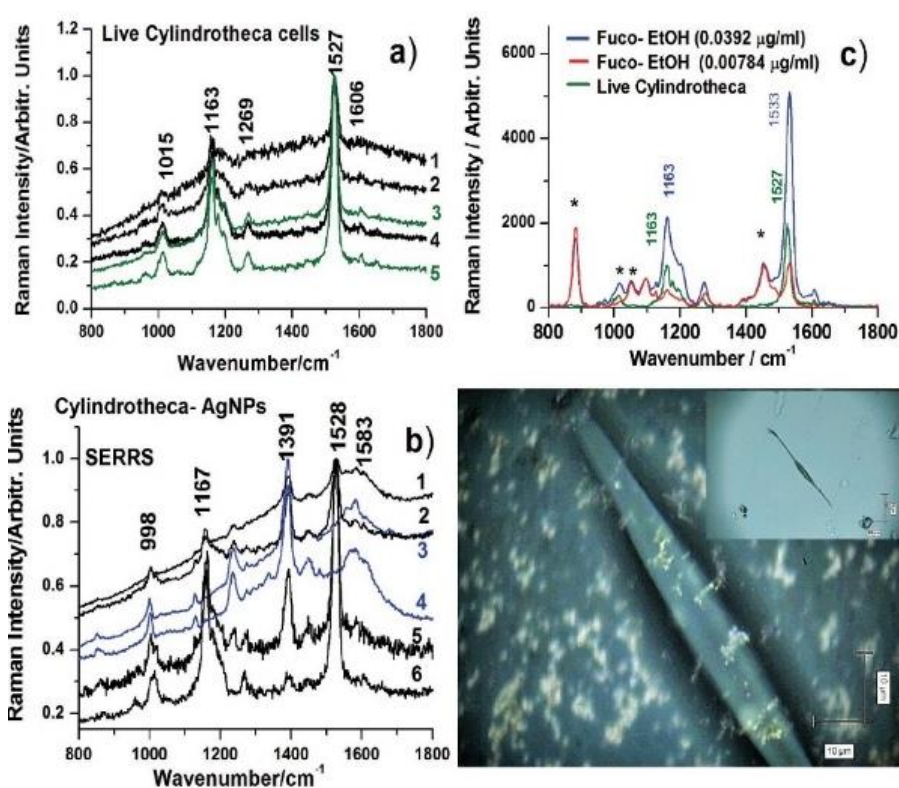


Figure 2.8 Resonance Raman spectra collected from five distinct live *C. closterium*, numbered 1 to 5: (a) obtained from greenish chloroplasts inside the cell body; (b) typical SERRS signals taken from living cells exposed to AgNPs, showing distinct responses, focusing on the cell surface, from the extracellular matrix on the cell (blue spectra) or from chloroplasts, focusing inside the cell (black spectra); (c) comparison of the position of the main mode of carotenoids in the *C. closterium* for two fucoxanthin solutions of different concentrations, asterisks indicate ethanol bands. Excitation: 532 nm. The inset shows a micrograph of a *C. closterium* cell exposed to AgNPs and the corner shows a live cell observed by light microscopy in diatom culture solution (Reproduced from F., I. Brezeștean, G. Lazar, C. Firța, S. Cînta Pînzaru, Volume 1250, Part 1, doi.

10.1016/j.molstruc.2021.131608, *J. Mol. Struct.*)

The unique feature of the fucoxanthin signal is the band around 1606 cm^{-1} , which corresponds to the out-of-plane C=C stretch present in the spectra from cells and whose intensity is a confirmation of the dominance of fucoxanthin among other carotenoids in cells.

Figure 2.8 clearly shows that the position of the specific band in the fucoxanthin solution at $1532\text{ cm}^{-1}/1527\text{ cm}^{-1}$. The SERRS band attributed to the C=C stretching mode was observed at 1528 cm^{-1} , but different cells showed a different band profile (or no band at all), equivalent to the 'dead' cells in the RR investigation. Thus, an estimate of carotenoid concentration based on SERRS intensity and C=C mode profile could only be considered with caution.

Chapter III. Structured nanoplatfoms for efficient SERS detection

III.1 3D nanoplatfoms fabricated by nanolithography

Nanoimprint Lithography (NIL) is a simple, reproducible and scalable method to create plasmonic nanostructures with diverse patterns and wide applicability, for example, for the fabrication of SERS substrates. NIL can overcome the limitations of other imprinting techniques, such as high cost, time consumption and highly equipped nanofabrication labs, by taking advantage of the roll-to-roll⁶⁵ method. NIL enables the production of various high-resolution periodic nanostructures on both hard and soft surfaces, such as plastics and flexible substrates: paper, plastic and other polymer sheets⁶⁶⁻⁶⁹.

The new 3D models have gained high interest, in particular due to their ability to significantly increase the detection area, allowing a higher density of plasmonic nanostructures and enabling highly reproducible, ultrasensitive and specific molecular detection⁷⁰. In this study, a new reproducible 3D nanostructured detection platform fabricated by the NIL technique with high sensitivity up to analyte concentrations of up to 10 pM was proposed. As a SERS substrate, we deposited Ag thin films with thicknesses ranging from 10 nm to 100 nm on an IPS® plastic substrate. To evaluate the SERS performance of flexible, transparent, imprinted Ag-coated substrates of four different thicknesses, we chose CV as the analyte. CV has well-established vibrational characteristics as a commonly used standard molecule and has been reported as an analyte in studies that have achieved monomolecule detection using SERS⁷¹⁻⁷³. As a novelty, in this work, the potential for SERS enhancement was explored by considering the synergy of three key aspects: the metalization of Ag, the effect of increasing Ag film thickness and the contribution to SERS amplification of periodic nanotrenches fabricated by NIL.

In our experiments we used a 4.5 cm × 4.5 cm Si die custom fabricated by the manufacturer using electron beam lithography (EBL). It consists of a 1 cm × 1 cm square surface containing a periodic lattice of equal-width (400 nm) nanolayers and nanogaps with a depth of 300 nm and a pitch of 800 nm. To prevent degradation and sticking, the matrix was subjected to a coating treatment with perfluorodecyltrichlorosilane, also known as FDTS as an anti-adhesive coating. **Figure 3.1** illustrates a step-by-step schematic protocol for fabrication of the patterned substrate and its subsequent use for SERS measurements.

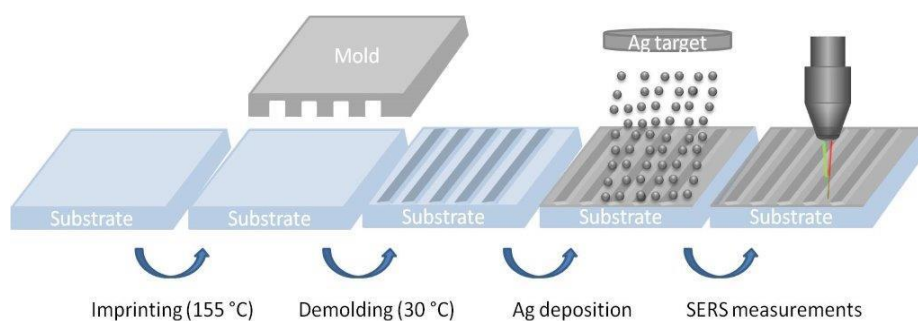


Figure 3.1 Schematic step-by-step protocol for fabrication of the printed substrate and its subsequent use for SERS measurements (Reproduced from A. Colniță, D. Marconi, N. E. Dina, I. Brezeștean, D. Bogdan, I. Turcu, Volume 276, /doi.org/10.1016/j.saa.2022.121232, Spectrochimica Acta Part A)⁷⁴.

The fabrication process involved, using thermal NIL, the same equipment and the same substrate, was presented in another study⁷⁵. Briefly, the IPS® substrate is heated to a temperature of 155 °C to make the polymeric substrate soft. **Figure 3.2** illustrates a scanning electron microscopy (SEM) image of the nanostructured patterned die and its architecture imprinted on an IPS® substrate. After cooling of the patterned substrate, Ag was deposited onto the patterned plastic using a Q150R PLUS deposition equipment (Quorum Technologies Ltd., Lewes, UK) from a disc-type Ag target (57 mm diameter, 0.1 mm thick).

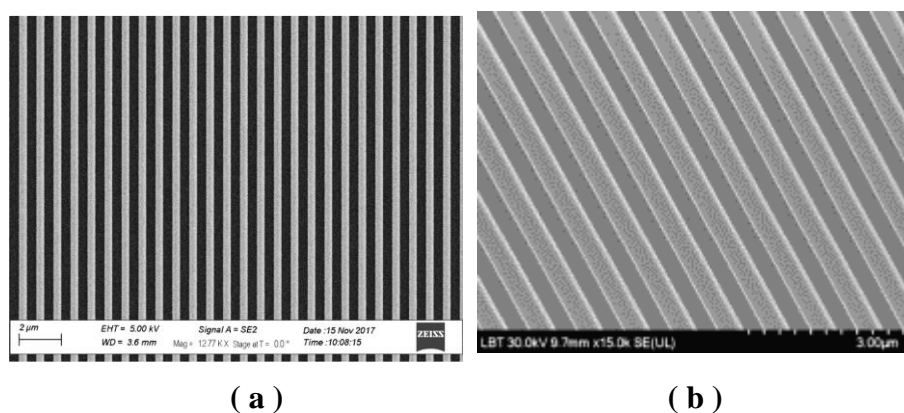


Figure 3.2. a) SEM image of the nanotrenches periodic pattern die used in the NIL imprinting technique (via NIL Technology ApS); b) SEM image of an imprinted IPS® substrate (Reproduced from A. Colniță, D. Marconi, N. E. Dina, I. Brezeștean, D. Bogdan, I. Turcu, Volume 276, /doi.org/10.1016/j.saa.2022.121232, Spectrochimica Acta Part A)⁷⁴

The morphology of the four samples of different Ag thicknesses was evaluated by SEM measurements, and representative micrographs are shown in **Figure 3.3**. It is remarkable that for all samples the Ag atoms formed uniform and granular films, with the Ag nanoclusters evenly distributed on the nanostructured and patterned plastic substrate. In the case of the 10 nm Ag thickness sample (**Figure 3.3a**) an irregular film with possibly discontinuous areas is formed. The grain size was estimated from the SEM image to be ≈ 20 nm. The granular appearance dominates the surface of the nanotrenches and the spaces between them. A film thickness of 25 nm (**Figure 3.3b**) provides the opportunity for Ag nanoclusters to connect and form a very thin and hard metallic substrate, with an average film size of 30 nm estimated from SEM images, which can fairly contribute to SERS enhancement. An additional Ag thickness increased to 50 nm (**Figure 3.3c**) contributes to reducing the distance between nanoclusters, increasing the roughness and increasing the size of Ag nanoclusters up to 35 nm. The uniform distribution on the top and bottom of tightly packed Ag granules (as further demonstrated by AFM measurements) leads to an increase in the surface-to-volume ratio of plasmonic nanostructures, as demonstrated⁷⁶.

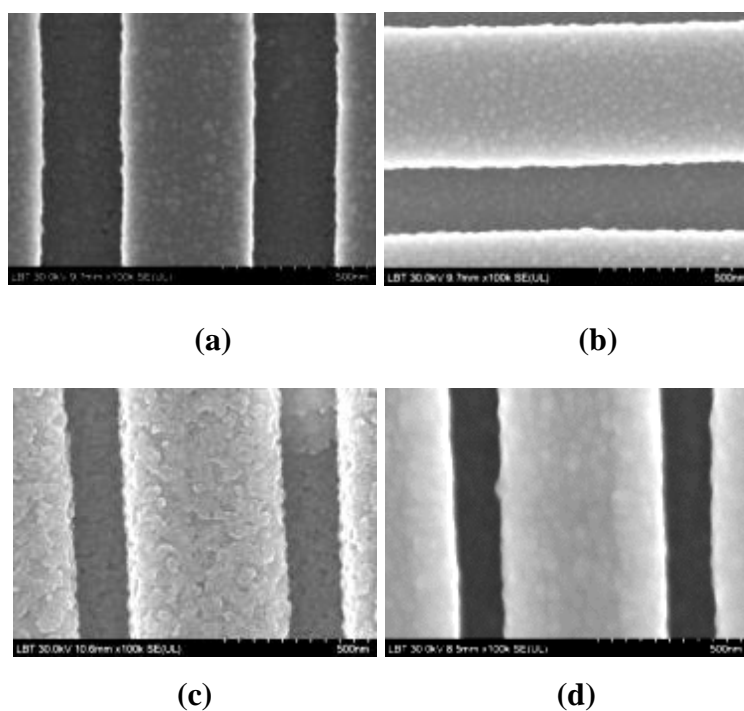


Figure 3.3 Representative SEM images of Ag-coated nanotrenches with films of (a) 10 nm; (b) 25 nm; (c) 50 nm and (d) 100 nm thickness, respectively. (Reproduced from A. Colniță, D. Marconi, N. E. Dina, I.

To demonstrate the SERS amplification potential of the Ag-coated nanoimprinted substrate, we first determined a detection limit for CV Raman analysis. For this, we used only the plastic substrate, with no pattern or Ag film deposited on its surface.

AFM characterization of ordered Ag-coated nanoplatfoms

Figure 3.4 shows AFM images of the four samples after Ag deposition. The coating is continuous and uniformly distributed on the nanotrenches. The pitch was evaluated from the section profiles and is constant (800 nm) for all four samples. On the contrary, the distance between two consecutive edges (indicated as distance *a* in **Figure 3.4D**) decreases from about 390 nm (for 10 nm Ag deposition) to about 310 nm (for 100 nm Ag deposition) due to the increased thickness of the metal layer. The morphology of the Ag layer was evaluated on a 400 nm trench surface and indicates a continuous layer consisting of overlapping grains of tens of nanometers in size, more precisely with a diameter of about 30 nm for 25 nm Ag thickness (inserted in **Figure 3.4B**).

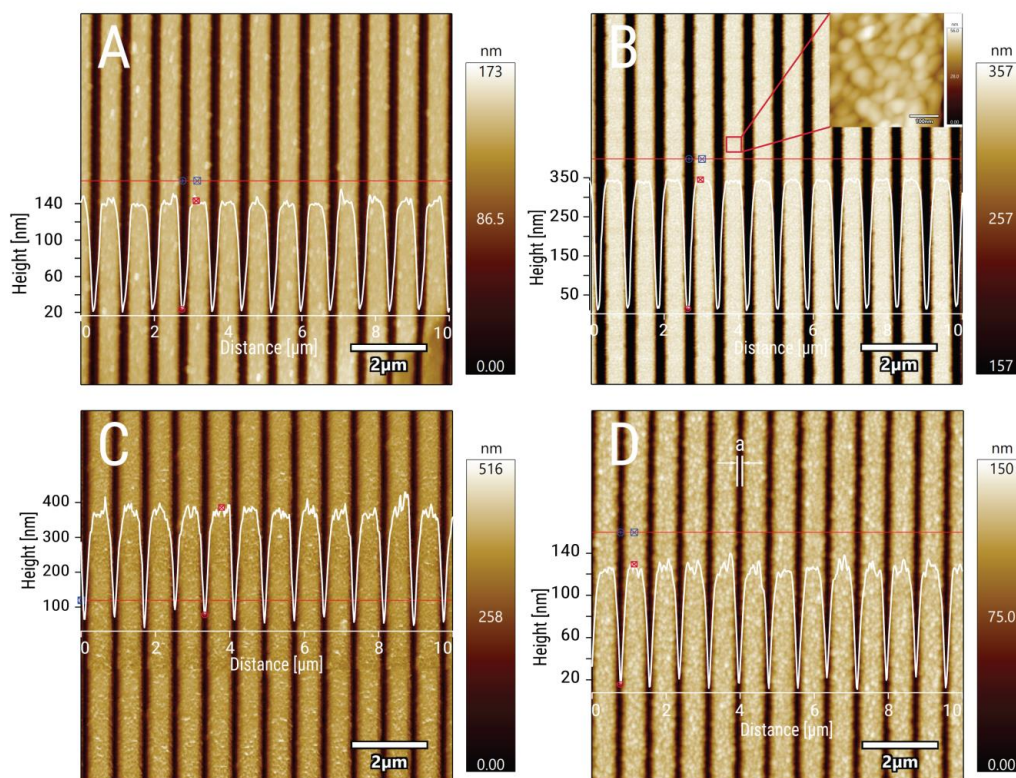


Figure 3.4. 2D AFM images (scan size 10 μm) of periodic trenches after deposition of 10 nm (A), 25 nm (B), 50 nm (C) and 100 nm (D) Ag, respectively, showing a continuous layer covering the substrate. The inset in B indicates the morphology (400 nm scan size) of the surface of the transitions. The section profiles correspond to

the red lines highlighted in the 2D images (Reproduced from A. Colniță, D. Marconi, N. E. Dina, I. Brezeștean, D. Bogdan, I. Turcu, Volume 276, /doi.org/10.1016/j.saa.2022.121232, Spectrochimica Acta Part A)⁷⁴.

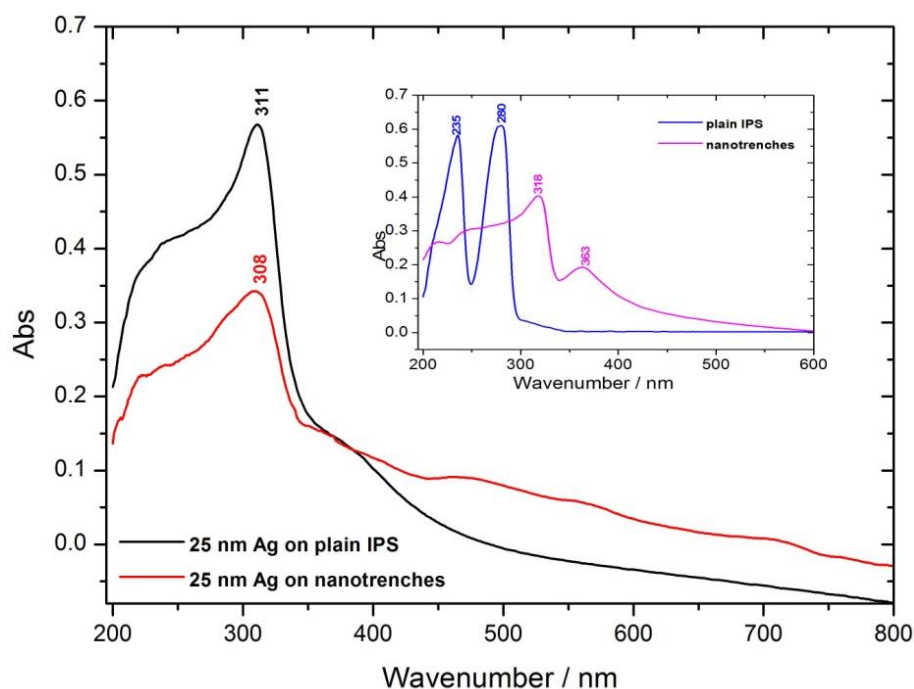


Figure 3.5. UV-Vis spectra on plain and printed IPS® with 25 nm Ag, with inset illustrating UV-Vis spectra on plain and printed IPS® substrate (Reproduced from A. Colniță, D. Marconi, N. E. Dina, I. Brezeștean, D. Bogdan, I. Turcu, Volume 276, /doi.org/10.1016/j.saa.2022.121232, Spectrochimica Acta Part A)⁷⁴.

UV-Vis analysis of plain IPS® samples and those patterned with the nanotrenches array is shown in **Figure 3.5**. The UV-Vis spectrum shows a minimal effect of the nanostructured area compared to the plastic substrate coated with a 25 nm thick Ag thin film. Thus, there is a blue shift from 311 nm to 308 nm and a broadening of the absorption band occurs. As shown in this figure, the hypochromic effect can be identified, as suggested in⁷⁷; taking into account that both IPS® substrates underwent a heat treatment during the patterning process, prior to Ag deposition, it can be concluded that the decrease in absorption is due to the presence of ordered nanotrenches. The inset in **Figure 3.5** shows the UV-Vis spectra of the plain plastic and the one imprinted with the nanotrenches lattice. The UV-Vis spectrum of plain IPS® has 2 strong bands at 235 nm and 280 nm. The UV-Vis spectrum of the area containing ordered nanotrenches is quite similar to the other two UV-Vis spectra of the Ag-based samples and has 2 peaks at 318 nm and 363 nm.

Our findings suggest that the 25 nm silver film covering the NIL-printed nanotrenches in plastic is the most promising of the 4 different Ag film thicknesses that were tested. The final

AEF obtained in this case was 1.7×10^7 , with a silver film contribution of only one order of magnitude.

The produced SERS substrates containing a 25 nm Ag film deposited on the imprinted nanotrenches exhibited a considerably improved and much more uniform plasmonic surface than other, thicker films. Specifically, SERS substrates with silver aggregates enabled SERS sensitivity for CV detection up to a limiting concentration of 10 pM. In addition, amplification factors between 2.3×10^5 and 1.7×10^7 were estimated when 4 other SERS marker bands were considered as reference. Our ultimate goal is to use these SERS substrates to develop optical biosensors for the detection of high-impact bacterial-specific molecules in *quorum sensing*.

III.2 Detection of cyanotoxin Nodularin

Cyanobacteria, also known as blue-green algae, although strictly speaking not algae, account for up to 70% of all phytoplankton biomass and are believed to be the first oxygenated photosynthetic microorganisms on Earth^{78,79}. They populate almost all marine and freshwater environments and use sunlight as an energy source to produce biomass from carbon dioxide (CO₂). In the absence of effective strategies to mitigate their overgrowth under eutrophic conditions (massive cyanobacterial blooms), water quality can be impaired by inducing toxicity in freshwater and marine environments. Furthermore, uncontrolled cyanobacterial growth can induce the release of toxins causing liver, digestive and neurological diseases through ingestion by living organisms⁸⁰⁻⁸³. Cyanobacteria produce potent toxins such as hepatotoxic microcystins (MC) and nodularins (NOD)⁸⁴⁻⁸⁶. MCs and NODs are hepta- and pentapeptides with very similar structures, which have been shown to cause hepatotoxicity by inhibiting phosphate proteins 1A and 2A (PP1 and PP2A) that lead to the intensive use of vital cellular proteins. After ingestion, these toxins are absorbed from the ileum into the bloodstream and processed by the liver via multispecific transmembrane organic anion transporters⁸⁷.

NODs are produced by the filamentous cyanobacterium *Nodularia spumigena*⁸⁸ and the benthic species *Nodularia sphaerocarpa* PCC7804⁸⁹⁻⁹¹. Their biosynthesis is regulated by genes and is carried out in a non-ribosomal manner, following a similar mechanism involved in the production of MCs⁹². Currently, ten structural variants of NODs are known⁹³. These types of protein-bound MCs have not been detected using well-known analytical approaches, so the actual MC content of cyanobacterial blooms has been underestimated⁹⁴.

Nowadays, three types of analytical methods are used to detect MC: biological, biochemical (enzyme-linked immunosorbent assay - ELISA) and chemical (high-performance

liquid chromatography - HPLC, liquid chromatography-mass spectrometry - LC-MS, high-performance capillary electrophoresis - HPCE and gas chromatography - GC)⁹⁵. Biological methods have serious limitations such as: lack of sensitivity, not suitable for quantification or routine and large-scale testing, require large numbers of guinea pigs^{96,97}.

SERS-based biosensors for the detection of MCs have proven to be fast, highly sensitive, non-destructive and easy to use. Recently, a new SERS immunosensor for the detection and quantification of MC-LR toxin in aquatic environments⁹⁸ with a detection limit of 0.014 µg/L was reported, while the same group subsequently developed a sensitive and selective aptasensor for dual fluorescence-SERS mode detection of MC-LR toxins⁹⁹.

In this study, we report the use of two highly sensitive spectroscopic techniques, DCDR and SERS for NOD detection and full assignment of its vibrational modes, in combination with DFT calculations. For DCDR analysis, we chose a commercial slide known as Tienta SpectRIM™, which provides a detection limit of up to 10⁻⁴ M. By using a commercial substrate with periodic pyramidal square dimpled nanopatterns (Klarite™), a SERS limit of detection (LOD) of 10⁻⁷ M was achieved. In-house fabricated periodic NIL nanotrenches, silver (Ag) nanostructured films with thicknesses of 25 nm obtained by direct current (DC) deposition were also tested. When a regular Ag sol was used for SERS analysis, an LOD of 58 pM was achieved. To the best of our knowledge, this is the first SERS study on NOD as a centerpiece reported to date.

III.2.1. Raman analysis of cyanotoxin Nodularin by DCDR (Drop Coating Raman Deposition)

As demonstrated in previous studies¹⁰⁰, DCDR analysis has shown superior detection sensitivity by the conventional Raman technique of small biological molecules such as acetylsalicylic acid, riboflavin and contaminants^{101,102} up to a detection limit of 10⁻⁸ M. Advantages of DCDR analysis include the use of dry, preconcentrated sample in a small sample volume, lack of solvent interference and the ability to segregate any existing impurities¹⁰³. Therefore, when signal acquisition occurs from the outer edge of the dried coffee ring droplet on a hydrophobic surface, a significantly enhanced Raman signal is detected.

Figure 3.6 shows the DCD Raman spectra obtained by using different laser lines as excitation sources on a Tienta® substrate. The marker bands are in good agreement with the Raman NOD profile reported in the literature¹⁰⁰ and show high reproducibility independent of the laser line. The most intense Raman bands are attributed to the phenylalanine amino acid - Phe (1003 cm⁻¹, the strongest band in the low wavenumber region, 823 cm⁻¹, 1208 cm⁻¹) or the

Adda group, common to all microcystins (1208 cm^{-1} , 1304 cm^{-1} , 1375 cm^{-1} , 1452 cm^{-1} , 1645 cm^{-1}), as shown by Halvorson *et al*¹⁰⁰.

The Raman bands observed at 1645 cm^{-1} are characteristic of amide I and around 1003 cm^{-1} are attributed to the phenyl ring in the Adda residue. Other marker bands present for the NOD molecule and previously reported in the literature are found in the range 1200 - 1300 cm^{-1} and are characteristic of Amide III. In contrast to previously reported studies¹⁰⁰, this paper describes spectral features found in the range 2700 - 3200 cm^{-1} . We could identify intense bands in the range 2880 - 3060 cm^{-1} , being characteristic of symmetric CH vibrations. In this case, a detection limit of only 10^{-3} M was reached, so we investigated other substrates with higher detection performance.

Thus, **Figure 3.6A** reveals the NOD spectrum on the commercial hydrophobic Tienta SpectRIM™ substrate, a hydrophobic slide. The 2 μl sample was deposited and allowed to air dry, then irradiated for Raman signal acquisition. The Raman spectra obtained for NOD recorded using three laser lines are almost identical to those obtained on the hydrophobic Tienta® substrate. **Figure 3.6B** shows the Raman spectra of NOD at a concentration of 10^{-4} M. By decreasing the concentration, the marker bands of NOD can still be clearly observed at 1003 cm^{-1} , 1376 cm^{-1} and the most intense band at 1644 cm^{-1} . In addition, we have attempted to achieve a lower detection limit by switching from commercial hydrophobic substrates to more efficient substrates SERS.

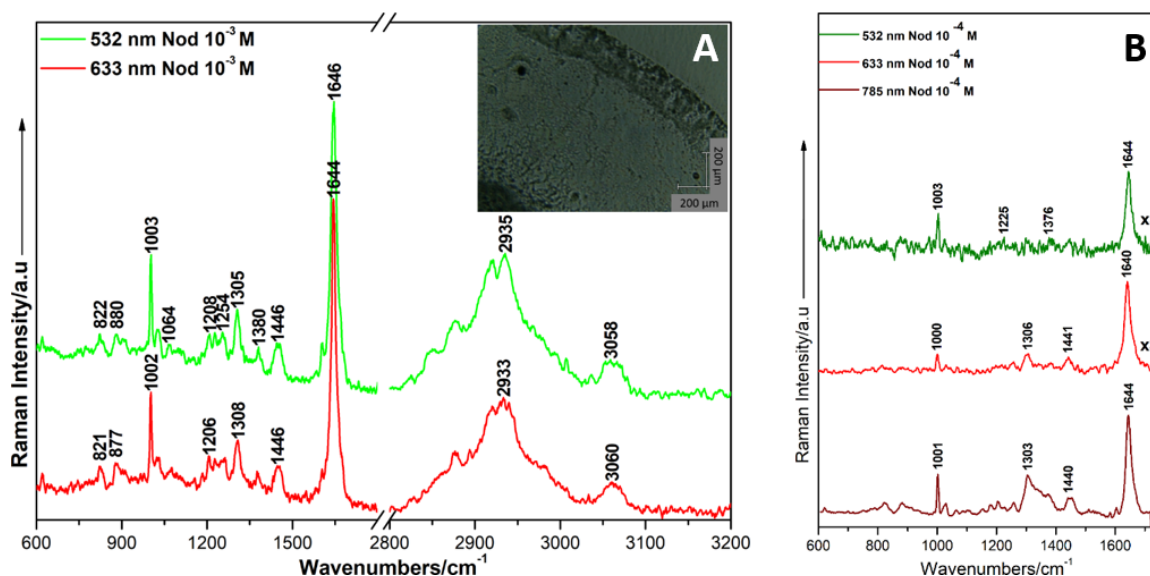


Figure 3.6 DCDR spectra of NOD recorded on the Tienta SpectRIM™ substrate for NOD in ethanol with a final concentration of 10^{-3} M (A) and 10^{-4} M (B), respectively, using 785 nm, 532 nm and 633 nm laser lines.

Inset optical image using the 20 \times .

III.2.2 SERS detection of cyanotoxin Nodularin

Figure 3.7 C shows the NOD spectra on the commercial SERS substrate Klarite at various concentrations up to 10^{-7} M. The Klarite substrate has previously been used successfully for label-free detection of bacteria ¹⁰⁴, highlighting its key aspects of SERS performance, such as a strong SERS signal under ambient conditions and ease of sample deposition on its surface. We used the same drop deposition on this substrate and aimed to achieve a detection limit below 10^{-4} M. In Figure 4.7 A and B we illustrate representative optical images of sample clusters formed after ethanol evaporation. We mainly investigated the edges of the "coffee ring", where visible NOD microcrystals are accumulated; therefore, an amplified Raman signal is expected.

A medium to strong SERS band is present at all concentrations tested at 1055 cm^{-1} . This spectral feature is particularly observed in SERS spectra recorded on the Klarite substrate. It is possible that the inverted periodic pyramids imprinted on this substrate forced NOD molecules to accumulate in their cavities in different geometrical configurations and thus molecular adsorption could have been performed in several orientations with respect to the silver.

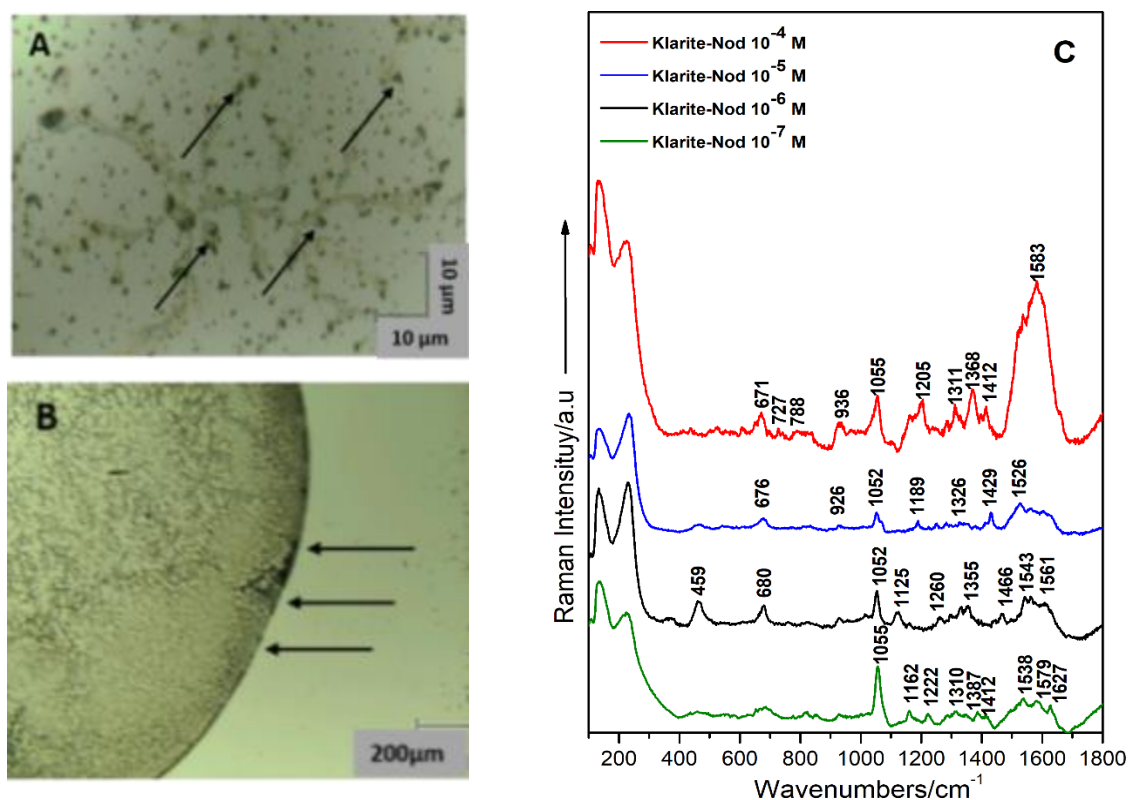


Figure 3.7. Optical images showing samples for Nodularin on Klarite substrate using $100\times$ (A) and $20\times$ (B) magnification. Arrows show selected spots for laser irradiation. SERS spectra recorded on Klarite substrate for Nodularin in ethanol at different concentrations using the 532 nm laser line (C).

Figure 3.8 shows systematic detection of NOD using AgNPs at different concentrations up to 10⁻¹² M. At low concentrations, SERS spectra show ethanol-specific bands: 878 cm⁻¹, 1045 cm⁻¹, 1087 cm⁻¹ and 1453 cm⁻¹ respectively. Despite this, from 10⁻¹² M concentration upwards, NOD-specific spectral features are increasingly visible. The band around 1365-1375 cm⁻¹ increases in intensity especially for the lowest LOD. The spectral range between 1500 cm⁻¹ and 1650 cm⁻¹ is also very abundant in features, especially the marker band for NOD found at 1645 cm⁻¹ becomes increasingly dominant in this region.

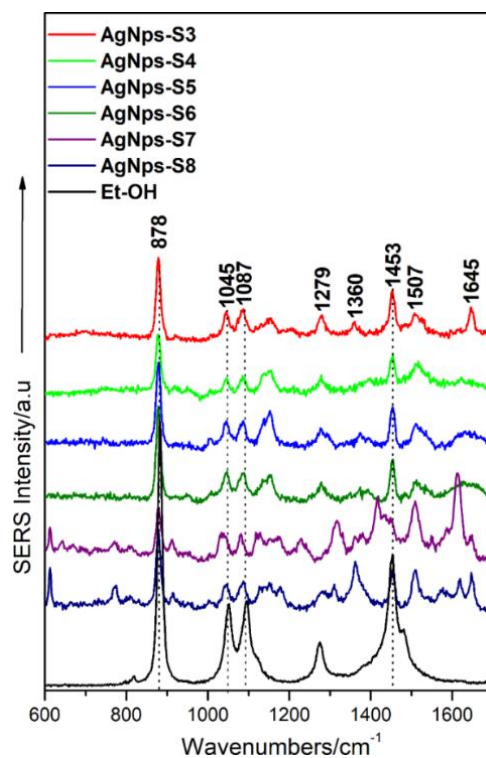


Figure 3.8. SERS spectra of NOD/ethanol samples at different concentrations using the 532 nm laser line and Lee-Meisel synthesized AgNPs.

A surprisingly intense and visible SERS band is observed compared to the dry drop measurement on solid substrates at 1507 cm⁻¹. Moreover, in Raman analysis this band is not significantly present. This could be explained by the tilted position of the molecule relative to the metal surface of the AgNPs.

This study focuses on the detection and characterization of cyanotoxin NOD using improved surface approaches based on Raman microspectroscopy. By DCDR was evaluated for NOD and was detected with a LOD of 10⁻⁴ M. SERS analysis was performed for NOD detection even at a level of 10⁻¹² M using AgNPs. We correlated the SERS marker bands in terms of intensity and position with the NOD-specific DCDR signal obtained at higher concentrations. Using different laser lines as excitation sources, we were able to detect NOD

with slightly shifted marker bands but with significant changes in intensity. Our experiments show that for label-free detection, physisorption alone, even if facilitated by sample preconcentration or by using high-performance solid SERS substrates, is not sufficient. By NOD adsorption on the silver surface and chemical interaction via key N groups, the SERS regime is fully achieved and an additional amplification of at least one order of magnitude is obtained.

III.3 Self-assembled colloidal silver nanoparticles on solid substrates

Pesticides are among the most dangerous chemicals that harm the environment and require strict monitoring ¹⁰⁵. Solid SERS substrates fabricated by advanced nanolithography methods, such as EBL, are excellent in terms of control over nanostructure morphology and versatility of optical properties required for SERS amplification. AuNPs and AgNPs, which generally have diameters between 10 and 200 nm, are easy to synthesize and can be used for the detection of pesticide residues and biotoxins ^{106,107}.

Thiabendazole (TBZ), a benzimidazole derivative, is one of the widely used pesticides that is also used as a fungicide to prevent mould, rot and fruit scorch. Although TBZ has low toxicity compared to other pesticides, it is associated with adverse effects including nephrotoxicity, hepatotoxicity, carcinogenicity and teratogenicity ¹⁰⁸. To measure TBZ residues in food samples ¹⁰⁹, a SERS method combined with a homogeneous and reusable gold nanorod array (GNR) substrate ¹⁰⁸ has been proposed. SERS has also been applied as an analytical technique to detect thiabendazole (TBZ) at low concentrations using Ag colloid ^{109,110}.

Endosulfan - (ES) is a broad-spectrum organochlorine pesticide that has been used on cereals, fruits, vegetables and cotton since the 1950s ^{111,112} and is also one of the most stable substances detected in the environment worldwide. It belongs to the category of persistent organic pollutants (POPs) ¹¹³ because of its bioaccumulation, its resistance to long-range transport and its negative effects on human health, ecosystems and aquatic systems ^{114,115}. In addition, the organochlorine pesticide ES was detected for the first time using SERS at low concentrations ¹¹⁶. Detection of organochlorine pesticides is still a major challenge due to their low affinity for metal surfaces.

In the following we report the fabrication of Ag films by convective self-assembly (CSA) of AgNPs synthesized by the Lee and Meisel method ¹¹⁷. After a morphological characterization by SEM, the films are evaluated as SERS substrate with para-aminothiophenol molecule (pATP) using three excitation laser lines. Subsequently, the possibility of using the fabricated AgNP films as substrates for SERS characterization of two types of pesticides,

thiabendazole (TBZ) and α -endosulfan (α -ES), is explored. AgNP films were optimized for surface functionalization and for better anchoring of the pesticides to the metal surface.

Specifically, two types of thiol molecules, hexanethiol (HT) and octanethiol (OT), were used in an attempt to improve the interaction between α -ES and the metal surface. In addition, we observed that the SERS signals of HT and OT recorded on AgNPs films provide clear spectral differences useful for their differentiation, despite the similarity of these two molecules. TEM images of the prepared colloidal AgNPs are shown in **Figure 4. 9(a)**. In addition to the spherical-shaped particles, many of them possessed an asymmetric rod-like shape. The size histogram showed a bimodal size distribution, with the majority of the particles having sizes around 40 nm, with an additional population having sizes around 60 nm. The UV/VIS extinction spectrum showed the characteristic band attributed to localized surface plasmon resonance, with a maximum at 424 nm.

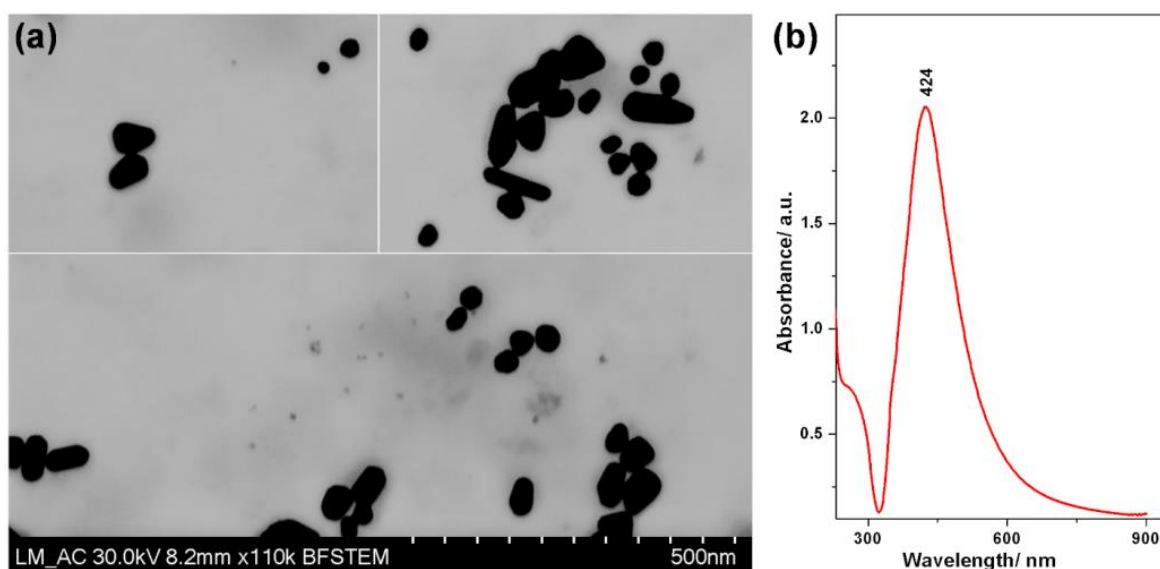


Figure 3.9 (a) TEM images of Ag nanoparticles. (b) Extinction spectrum of the colloidal suspension of synthesized Ag nanoparticles.

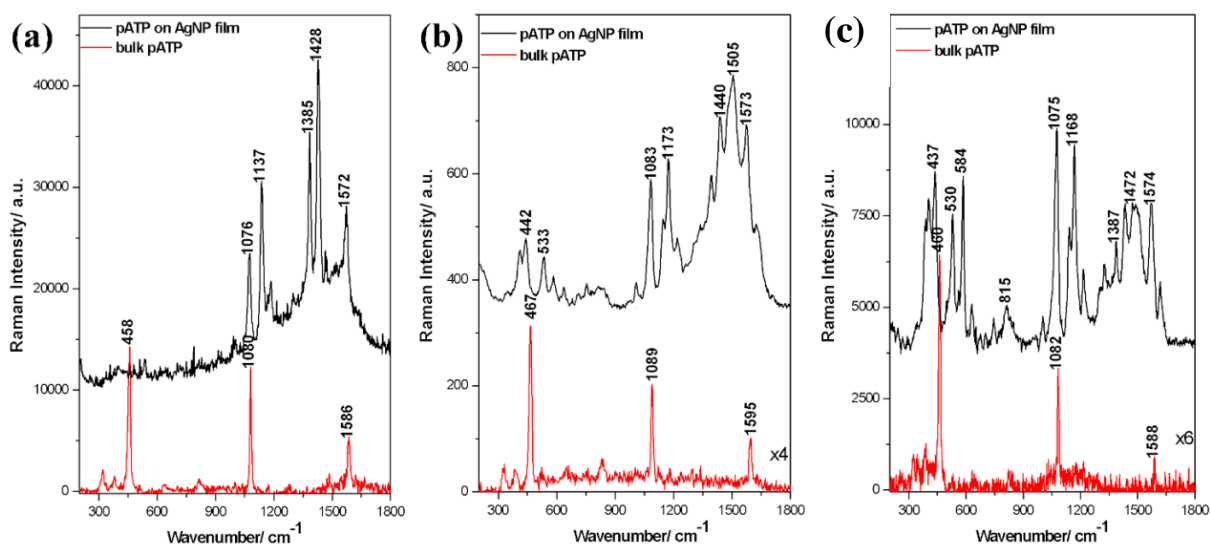


Figure 3.10 SERS spectra of p-ATP adsorbed on AgNP films and Raman spectra of p-ATP powder obtained at different laser excitations: (a) 532 nm, (b) 633 nm, (c) 785 nm.

Figure 3.10 shows typical SERS spectra of the p-ATP molecule on AgNP films recorded at three different commonly used laser lines, together with the corresponding Raman spectra of p-ATP.

III.3.1 SERS detection of thiabendazole fungicide

AgNPs films were subsequently used for the identification and SERS characterization of TBZ pesticide. Spectra were acquired from different points on the sample surface and are shown in **Figure 3.11**. The spectral features observed were very similar in all spectra, highlighting the good reproducibility provided by the substrate developed. The main bands identified are located at 782, 884, 929, 1009, 1280, 1375, 1432, 1545 and 1579 cm^{-1} . We calculated the average SERS spectra characteristic of the TBZ-immersed AgNP film and the AgNPs film, respectively, and calculated their differential spectra (**Figure 3.11b**) to clearly identify the spectral characteristics of TBZ. In addition, the differential spectrum is compared with the Raman spectrum obtained from the powder and the TBZ spectrum calculated by DFT.

For example, following subtraction, the 1000 cm^{-1} band characteristic of the polystyrene substrate was properly removed and the fingerprint bands of TBZ located around 992 and 1009 cm^{-1} were highlighted. Vibrational spectral analysis was further performed based on experimental data and DFT calculations. The calculated vibrational wavenumbers and Raman activities were used to explicitly identify vibrational modes. Accordingly, the main characteristic TBZ bands can be detected in SERS spectra and assigned to specific vibrations. The main bands identified here are located at 782, 1009, 1280, 1545 and 1579 cm^{-1} . Other

intense Raman bands such as those at 987 and 1491 cm^{-1} appeared diminished in the SERS spectra. The 987 cm^{-1} was visible as a shoulder, mainly in the calculated differential spectra, while the 1491 cm^{-1} , corresponding to the C - N stretching vibrations in the thiazole ring, shifted blue to 1432 cm^{-1} and its relative intensity was substantially reduced. Analyzing the SERS main intensity bands, we can assume that TBZ molecules are adsorbed on the silver surface via the π electrons of the benzene ring, similar to other previous investigations¹¹⁸.

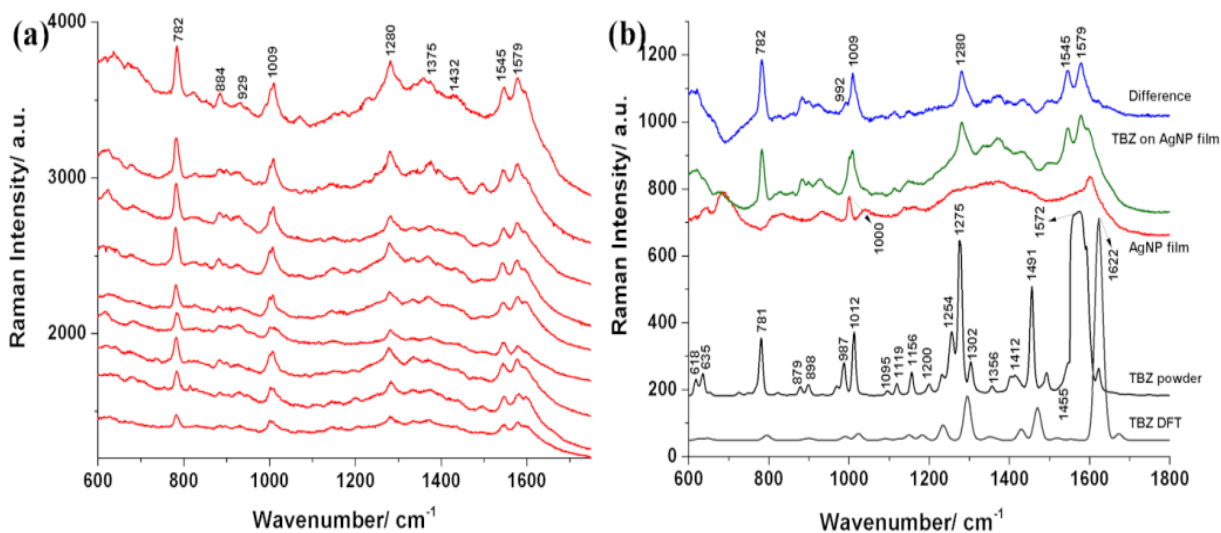


Figure 3.11 (a) SERS spectra of TBZ on AgNPs film collected from different locations on the substrate. Excitation 785 nm. (b) Raman spectra of TBZ powder and Raman spectra calculated by DFT compared with Raman spectra of AgNPs film, SERS spectra of TBZ on films and their calculated differential spectra.

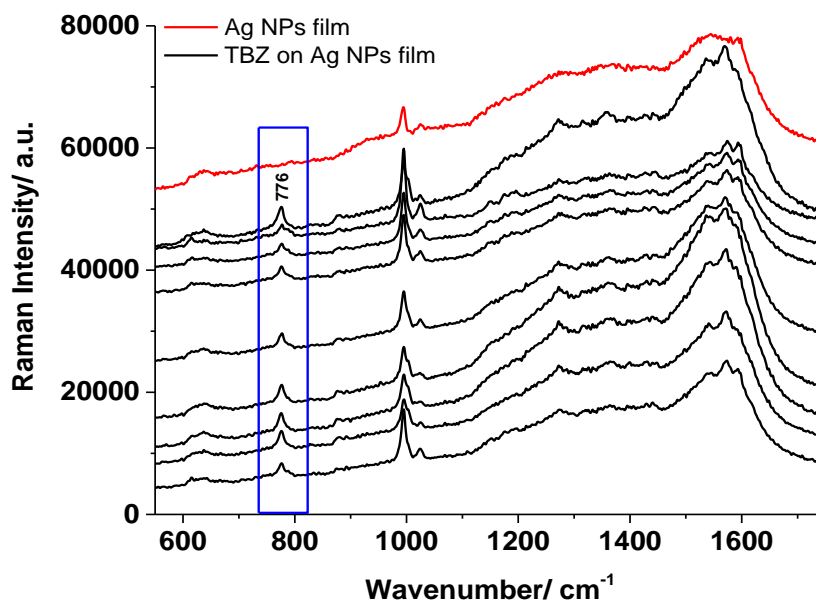


Figure 3.12 SERS spectra of TBZ recorded on AgNP film and AgNP film using a portable Raman spectrometer (532 nm)

The aim of this experiment was to determine whether AgNPs films could be used for future field experiments. In such applications, compact and portable Raman systems, which are not as powerful as Raman spectrometers, should be used. **Figure 3.12** shows several spectra obtained from TBZ adsorbed on AgNP film. The laser line used for excitation was 532 nm and even though the AgNP films showed the lowest amplification factor for this excitation wavelength, TBZ could be detected. The TBZ marker band at 776 cm^{-1} was observed in all spectra collected from different locations of the AgNP film. In addition, a good reproducibility of the SERS spectra can be observed. Other characteristic TBZ bands identified in the spectra are located at 1271, 1449 and 1572 cm^{-1} . In addition, two faint bands are detected at 985 and 1003 cm^{-1} , attributed to the thiazole ring that respines, respectively, the C - C stretch of the benzene ring. However, their unambiguous identification is hampered due to overlaps caused by the 995 and 1024 cm^{-1} bands also observed on the film. As seen from measurements at 785 nm, these bands are characteristic of the polystyrene support substrate. Therefore, a better identification of the two TBZ bands located in this spectral region is obtained by subtracting the AgNP film from the spectrum of the film immersed in the TBZ solution. The good reproducibility of SERS spectra characteristic of TBZ adsorbed on AgNPs films obtained in this study suggests that these films can be used for its detection even under 532 nm laser line excitation conditions, despite the lower amplification exhibited by the substrates under these conditions. Furthermore, it is suggested that AgNP films could be used to detect TBZ pesticide in the field at possible contaminated sites.

III.3.2 SERS detection of endosulfan insecticide

Endosulfan (ES) is an organochlorine pesticide that has poor affinity for metal surfaces. Therefore, various approaches to capture ES near metal surfaces by chemical functionalization of SERS¹¹⁹ substrates have been explored. Self-assembled monolayer systems with thiol alkanes offer a versatile method of modifying metal surfaces to create molecular "pockets" between alkyl chains and the plasmonic surface¹²⁰. Therefore, ES pesticide molecules could be trapped near the plasmonic substrate surface by their hydrophobic interaction with alkane thiols, which would allow their detection by SERS¹²¹. The sensitivity of SERS is generally influenced by the chain length of alkanethiols¹²². Thus, alkane thiols with different chain lengths, such as hexane thiols (C6, HT) and octane thiols (C8, OT) were used in this work. The functionalization of AgNP substrate with HT and OT was confirmed by SERS spectra **Figure 3.13**, and the corresponding Raman spectra.^{122,123} were used for comparison in this work¹²⁴. Upon adsorption of HT and OT on the AgNP film surface, evidence of their chemisorption is based on the lack

of S - H stretching vibration (ν) at about 2575 cm^{-1} ¹²⁰. Evidence for thiolate-Ag bonding is evidenced by the vibrational behavior in the $\nu(\text{C-S})$ spectral region, along with $\nu(\text{C-C})$ and $\nu(\text{C-H})$. The two $\nu(\text{C-S})$ bands for both HT and OT upon adsorption on the Ag surface were observed in the $600\text{-}750\text{ cm}^{-1}$ frequency region, being shifted to much lower frequencies than those in pure alkane thiols¹²⁵. These vibrations are attributed to "gauche" (G) and "trans" (T) conformations around the two carbon atoms adjacent to the S atom (thiol group facing the Ag surface). The band at 635 cm^{-1} corresponds to G $\nu(\text{C-S})$ conformers and that at 700 cm^{-1} to T $\nu(\text{C-S})$ conformers for both HT and OT, the low frequency band being well defined only in the case of small chain alkane thiolates such as HT¹²³.

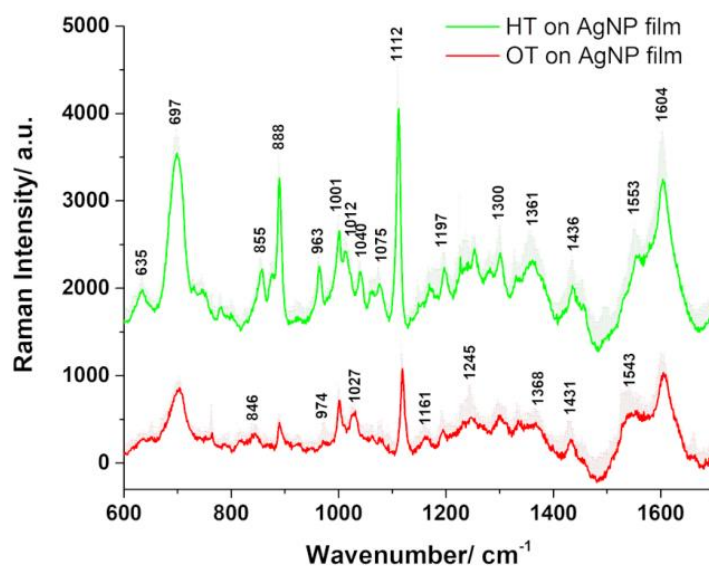


Figure 3.13. Average SERS spectra of HT- and OT-functionalized AgNP films, plotted together with their positive standard deviations, obtained under excitation at 633 nm.

The methylene wagging and deformation vibrations occurred in the wavenumber spectral region above 1300 cm^{-1} . The C-H vibrations show a quadratic correlation with the number of carbon atoms in the¹²² backbone. For example, in the case of the OT-functionalized film, the CH₃ swing vibrations exhibited a lower relative band intensity ratio of 888 cm^{-1} versus 857 cm^{-1} compared to the HT case, in direct correlation with the influence of the longer alkyl chain length and hydrophobic interactions between the chains. Pesticide ES is an asymmetric molecule containing a rigid norbornene unit connected via an HC₅-C₆H bridge to a seven-membered flexible aliphatic ring unit (**Figure 4.14**), in which only the two methylene groups (CH₂) and the sulfite group (SO₃) can induce changes in its conformation¹²⁶.

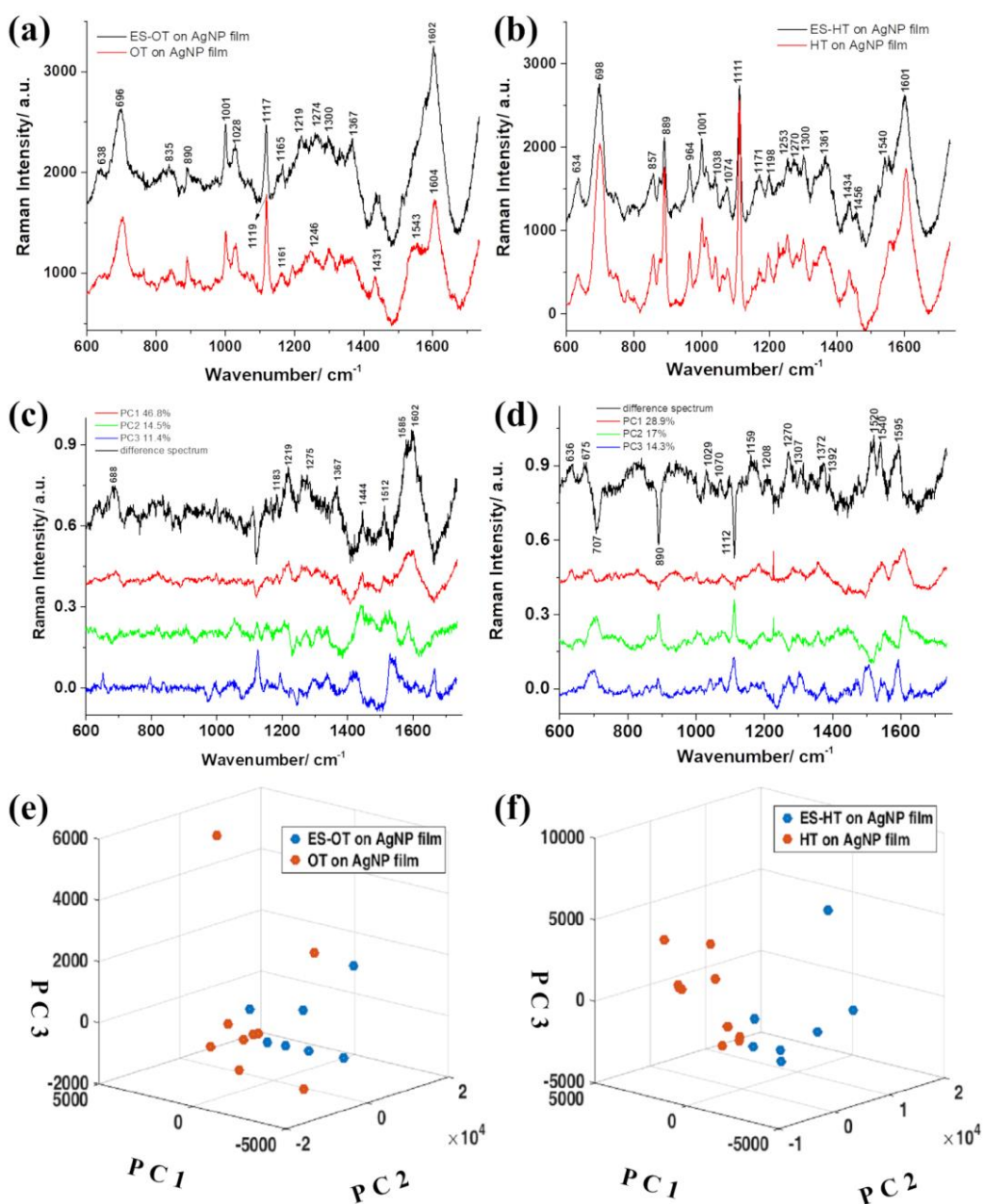


Figure 3.14 Average Raman spectra plotted for (a) ES-OT, respectively OT on AgNPs film and (b) ES-HT, respectively HT on AgNPs film . Loadings of the first three PCs and calculated difference spectra corresponding to ligands (c) OT, respectively (d) HT. 3D representation of the two groups of spectra for (e) OT, respectively (f) HT case.

The SERS spectrum of ES cannot be observed on AgNP, most likely due to the low affinity of ES for the rough Ag surface. Thus, the α -isomer of ES was analyzed in its pure form in solid form and then deposited by immersion of the monoalkanethiol-functionalized AgNP film, namely HT and OT. AgNP films functionalized with endosulfan-octan-thiol (ES-OT) or endosulfan-hexan-thiol (ES-HT) were analyzed and the results are shown in **Figure 4.14**.

The SERS spectra shown on films functionalized with ES-OT, ES-HT respectively appeared similar to those shown on films functionalized only with the respective thiol molecules. On closer inspection, however, slight differences can be identified. SERS spectral data for ES-coated films showed weakening of some bands associated with Ag-linked monothiols, as well as the appearance of several bands that may be associated with ES. Assignment of ES vibrations both in the solid state and on thin films of HT/OT functionalized AgNPs was performed based on general published data^{112,116,127} as well as theoretical calculations performed in this study.

Background interference from HT- and OT-functionalized AgNPs films, respectively, was subtracted from the ES-immersed AgNPs spectra, leading to the appearance of negative bands in certain regions of the spectra.

Analyzing the SERS spectra acquired from the ES-HT AgNPs film in comparison to the HT-AgNPs film, several attenuations of band intensity could be observed.

PCA was applied on the data set consisting of Raman spectra obtained from ES-OT and OT functionalized AgNPs films. The first three PCs accounted for a variance of 72.8%, and the loadings are shown in *Figure 4.23 c*. The PCs were used to differentiate the two films, and the 3D plot showing the separation and clustering of the spectra is shown in *Figure 4.23 e*. Separation was achieved using mainly PC1, but PC2 also showed good separation ability. Loading PC1, which accounted for 46.8% variation in the data set, showed similar characteristics to the difference spectrum calculated by subtracting the average Raman spectrum of the OT-functionalized AgNP film from the average Raman spectrum characteristic of the ES-OT-functionalized AgNP film? The main features included the following Raman bands: 630, 690, 857, 1070, 1147, 1147, 1183, 1219, 1259, 1275, 1367, 1444, 1512, 1585 and 1602 cm⁻¹.

Our results indicate that the longer alkane chains of OT allowed more efficient capture of ES molecules compared to the shorter HT chains, leading to a better SERS response. Due to the weak interaction between the alkane chains in the thiol monolayers, their assembly is rather compact, reducing the possibility of a direct interaction of the pesticide with the metal surface. However, adsorbed HT should exhibit a more disordered structure compared to OT, which has a longer chain and favours an increase in aliphatic chain order¹²⁰. More ordered OT films could lead to better anchoring of ES molecules near the SERS substrate.

Final conclusions

- ✓ This work aimed to implement Raman and SERS spectroscopy in the specific and quantisation detection of biomolecules of interest in environmental monitoring applications. The following main conclusions were drawn from the studies performed:
- ✓ We reported Raman and FT-IR fingerprints assigned to monosaccharide species found in different proportions as composing HePS purified from *A. platensis* cultures, identified as rhamnose, D(+)-glucose and D(+)-galactose. For conventional analyses, each compound must be extracted, purified and quantified separately. Thus, Raman microscopy offers a substantial reduction in time and labour while preserving information on the relative ratios of biochemical compounds at the level of individual cells. ***The final aim of this study was achieved by identifying exploitable bioresources that could be further exploited as an industrial quality building block.***
- ✓ ***SERS analyses of natural mineral waters*** have revealed the technique's ability to assess both organic and inorganic components, making it suitable for implementing sustainable carbonated spring water management. Mineral waters induced aggregation of AgNPs and provided a SERS fingerprint characteristic of beta-carotene.
- ✓ ***SERS sensing of individual cells and diatoms (C. closterium)*** with adsorbed AgNPs allowed for the detection of extracellular polymeric signals. Typical bands were assigned to polyunsaturated fats, together with a specific SERS contribution from carotenoids and chlorophylls. The three types of AgNPs used showed distinct interaction with diatom cells. Compact and portable Raman equipment provided good reproducibility for assessing carotenoid content in diatoms in batch cultures by normal Raman scattering.
- ✓ ***The rapid and cost-effective quantification of fucoxanthin in solutions is well supported in either Resonant Raman spectroscopy or SERRS, depending on the fucoxanthin concentration range to be detected.***
- ✓ ***The rapid increase in concentration or accumulation of certain microscopic algal species leads to drastic physico-chemical and biological changes in real aquatic ecosystems, and these changes are expected to be measurable by the SERS technique. Therefore, the contribution of individual species to the overall SERS signal is essential.***
- ✓ In this section, 3D SERS-active substrates were developed by depositing Ag films on nanopatterned plastic substrates fabricated by NIL. The contribution of both Ag film and nanopatterned structures in the final AEF obtained was determined. The effect of Ag nanoclusters induced by deposition in DC, only gives an enhancement of at most 10^2 . When

Ag films are deposited on the nanopatterned substrate, the synergistic enhancement effect is 7 orders of magnitude. Our findings suggest that the 25 nm silver film covering NIL-printed nanotrenches in plastic is the most promising of the 4 different Ag film thicknesses that were tested. The final AEF obtained in this case was 1.7×10^7 , with a silver film contribution of only one order of magnitude.

- ✓ The second part of the chapter focuses on the detection and characterization of cyanotoxin NOD using Raman microspectroscopy and SERS. By DCDR NOD was detected with an LOD of 10^{-4} M. SERS analysis was performed for the detection of NOD even at a level of 10^{-12} M using AgNPs.
- ✓ SERS substrates fabricated by CSA of AgNPs on solid planar substrates were evaluated on their SERS activity for pATP molecule using several excitation laser lines (532 nm, 633 nm, 785 nm). The films show the best SERS amplification factors for 785 nm, reaching values higher than 10^5 . The usefulness of these AgNP films for SERS detection of two types of pesticides, the fungicide thiabendazole and the insecticide α -endosulfan, was then demonstrated. These results are a step towards the development of SERS-based sensors for pesticide detection, identification and monitoring.

References:

- (1) Lee, P. C.; Meisel, D. Adsorption and Surface-Enhanced Raman of Dyes on Silver and Gold Sols. *J. Phys. Chem.* **1982**, *86* (17), 3391–3395. <https://doi.org/10.1021/j100214a025>.
- (2) Leopold, N.; Lendl, B. A New Method for Fast Preparation of Highly Surface-Enhanced Raman Scattering (SERS) Active Silver Colloids at Room Temperature by Reduction of Silver Nitrate with Hydroxylamine Hydrochloride. *J. Phys. Chem. B* **2003**, *107* (24), 5723–5727. <https://doi.org/10.1021/jp027460u>.
- (3) Lai, K.; Zhang, Y.; Du, R.; Zhai, F.; Rasco, B. A.; Huang, Y. Determination of Chloramphenicol and Crystal Violet with Surface Enhanced Raman Spectroscopy. *Sens. & Instrumen. Food Qual.* **2011**, *5* (1), 19–24. <https://doi.org/10.1007/s11694-011-9106-8>.
- (4) Tahir, M. A.; Dina, N. E.; Cheng, H.; Valev, V. K.; Zhang, L. Surface-Enhanced Raman Spectroscopy for Bioanalysis and Diagnosis. *Nanoscale* **2021**, *13* (27), 11593–11634. <https://doi.org/10.1039/D1NR00708D>.
- (5) Ortiz, C.; Zhang, D.; Xie, Y.; Ribbe, A. E.; Ben-Amotz, D. Validation of the Drop Coating Deposition Raman Method for Protein Analysis. *Analytical Biochemistry* **2006**, *353* (2), 157–166. <https://doi.org/10.1016/j.ab.2006.03.025>.
- (6) Al-Otaibi, J. S.; Albrycht, P.; Mary, Y. S.; Mary, Y. S.; Książopolska-Gocalska, M. Concentration-Dependent SERS Profile of Olanzapine on Silver and Silver-Gold Metallic Substrates. *Chem. Pap.* **2021**, *75* (11), 6059–6072. <https://doi.org/10.1007/s11696-021-01783-9>.
- (7) Mosier-Boss, P. Review of SERS Substrates for Chemical Sensing. *Nanomaterials* **2017**, *7* (6), 142. <https://doi.org/10.3390/nano7060142>.
- (8) Mosier-Boss, P. Review on SERS of Bacteria. *Biosensors* **2017**, *7* (4), 51. <https://doi.org/10.3390/bios7040051>.
- (9) Freitas, F.; Alves, V. D.; Reis, M. A. M. Advances in Bacterial Exopolysaccharides: From Production to Biotechnological Applications. *Trends in Biotechnology* **2011**, *29* (8), 388–398. <https://doi.org/10.1016/j.tibtech.2011.03.008>.
- (10) Nešić, A.; Cabrera-Barjas, G.; Dimitrijević-Branković, S.; Davidović, S.; Radovanović, N.; Delattre, C. Prospect of Polysaccharide-Based Materials as Advanced Food Packaging. *Molecules* **2019**, *25* (1), 135. <https://doi.org/10.3390/molecules25010135>.
- (11) Wang, J.; Hu, S.; Nie, S.; Yu, Q.; Xie, M. Reviews on Mechanisms of *In Vitro* Antioxidant Activity of Polysaccharides. *Oxidative Medicine and Cellular Longevity* **2016**, *2016*, 1–13. <https://doi.org/10.1155/2016/5692852>.
- (12) Laurienzo, P. Marine Polysaccharides in Pharmaceutical Applications: An Overview. *Marine Drugs* **2010**, *8* (9), 2435–2465. <https://doi.org/10.3390/md8092435>.
- (13) Rahbar Saadat, Y.; Yari Khosroushahi, A.; Pourghassem Gargari, B. A Comprehensive Review of Anticancer, Immunomodulatory and Health Beneficial Effects of the Lactic Acid Bacteria Exopolysaccharides. *Carbohydrate Polymers* **2019**, *217*, 79–89. <https://doi.org/10.1016/j.carbpol.2019.04.025>.
- (14) Xu, J.; Yue, R.-Q.; Liu, J.; Ho, H.-M.; Yi, T.; Chen, H.-B.; Han, Q.-B. Structural Diversity Requires Individual Optimization of Ethanol Concentration in Polysaccharide Precipitation. *International Journal of Biological Macromolecules* **2014**, *67*, 205–209. <https://doi.org/10.1016/j.ijbiomac.2014.03.036>.
- (15) Dina, N. E.; Leş, A.; Baricz, A.; Szöke-Nagy, T.; Leopold, N.; Sârbu, C.; Banciu, H. L. Discrimination of Haloarchaeal Genera Using Raman Spectroscopy and Robust Methods for Multivariate Data Analysis: Discrimination of Haloarchaeal Genera. *J. Raman Spectrosc.* **2017**, *48* (8), 1122–1126. <https://doi.org/10.1002/jrs.5187>.

- (16) McEwen, G. D.; Wu, Y.; Zhou, A. Probing Nanostructures of Bacterial Extracellular Polymeric Substances versus Culture Time by Raman Microspectroscopy and Atomic Force Microscopy. *Biopolymers* **2010**, *93* (2), 171–177. <https://doi.org/10.1002/bip.21315>.
- (17) Noack, K.; Eskofier, B.; Kiefer, J.; Dilk, C.; Bilow, G.; Schirmer, M.; Buchholz, R.; Leipertz, A. Combined Shifted-Excitation Raman Difference Spectroscopy and Support Vector Regression for Monitoring the Algal Production of Complex Polysaccharides. *Analyst* **2013**, *138* (19), 5639. <https://doi.org/10.1039/c3an01158e>.
- (18) Brezeştean, I.; Bocăneală, M.; Gherman, A. M. R.; Porav, S. A.; Kacsó, I.; Rakosy-Tican, E.; Dina, N. E. Spectroscopic Investigation of Exopolysaccharides Purified from *Arthrospira Platensis* Cultures as Potential Bioresources. *Journal of Molecular Structure* **2021**, *1246*, 131228. <https://doi.org/10.1016/j.molstruc.2021.131228>.
- (19) De Gelder, J.; De Gussem, K.; Vandenabeele, P.; Moens, L. Reference Database of Raman Spectra of Biological Molecules. *J. Raman Spectrosc.* **2007**, *38* (9), 1133–1147. <https://doi.org/10.1002/jrs.1734>.
- (20) Verrier, S.; Notingher, I.; Polak, J. M.; Hench, L. L. In Situ Monitoring of Cell Death Using Raman Microspectroscopy. *Biopolymers* **2004**, *74* (1–2), 157–162. <https://doi.org/10.1002/bip.20063>.
- (21) Wiercigroch, E.; Szafranec, E.; Czamara, K.; Pacia, M. Z.; Majzner, K.; Kochan, K.; Kaczor, A.; Baranska, M.; Malek, K. Raman and Infrared Spectroscopy of Carbohydrates: A Review. *Spectrochimica Acta Part A: Molecular and Biomolecular Spectroscopy* **2017**, *185*, 317–335. <https://doi.org/10.1016/j.saa.2017.05.045>.
- (22) Sathiyarayanan, G.; Yi, D.-H.; Bhatia, S. K.; Kim, J.-H.; Seo, H. M.; Kim, Y.-G.; Park, S.-H.; Jeong, D.; Jung, S.; Jung, J.-Y.; Lee, Y. K.; Yang, Y.-H. Exopolysaccharide from Psychrotrophic Arctic Glacier Soil Bacterium *Flavobacterium* Sp. ASB 3-3 and Its Potential Applications. *RSC Adv.* **2015**, *5* (103), 84492–84502. <https://doi.org/10.1039/C5RA14978A>.
- (23) Peng, X.-B.; Li, Q.; Ou, L.-N.; Jiang, L.-F.; Zeng, K. GC–MS, FT-IR Analysis of Black Fungus Polysaccharides and Its Inhibition against Skin Aging in Mice. *International Journal of Biological Macromolecules* **2010**, *47* (2), 304–307. <https://doi.org/10.1016/j.ijbiomac.2010.03.018>.
- (24) Xu, H.; Yu, G.; Jiang, H. Investigation on Extracellular Polymeric Substances from Mucilaginous Cyanobacterial Blooms in Eutrophic Freshwater Lakes. *Chemosphere* **2013**, *93* (1), 75–81. <https://doi.org/10.1016/j.chemosphere.2013.04.077>.
- (25) Li, W.; Ji, J.; Chen, X.; Jiang, M.; Rui, X.; Dong, M. Structural Elucidation and Antioxidant Activities of Exopolysaccharides from *Lactobacillus Helveticus* MB2-1. *Carbohydrate Polymers* **2014**, *102*, 351–359. <https://doi.org/10.1016/j.carbpol.2013.11.053>.
- (26) Stuart, R. K.; Mayali, X.; Lee, J. Z.; Craig Everroad, R.; Hwang, M.; Bebout, B. M.; Weber, P. K.; Pett-Ridge, J.; Thelen, M. P. Cyanobacterial Reuse of Extracellular Organic Carbon in Microbial Mats. *ISME J* **2016**, *10* (5), 1240–1251. <https://doi.org/10.1038/ismej.2015.180>.
- (27) Sevelsted, T. F.; Herfort, D.; Skibsted, J. ¹³C Chemical Shift Anisotropies for Carbonate Ions in Cement Minerals and the Use of ¹³C, ²⁷Al and ²⁹Si MAS NMR in Studies of Portland Cement Including Limestone Additions. *Cement and Concrete Research* **2013**, *52*, 100–111. <https://doi.org/10.1016/j.cemconres.2013.05.010>.
- (28) Cintă Pinzaru, S.; Müller, Cs.; Tomšić, S.; Venter, M. M.; Cozar, B. I.; Glamuzina, B. New SERS Feature of β -Carotene: Consequences for Quantitative SERS Analysis: New SERS Feature of β -Carotene. *J. Raman Spectrosc.* **2015**, *46* (7), 597–604. <https://doi.org/10.1002/jrs.4713>.
- (29) Rivas, L.; Sanchez-Cortes, S.; García-Ramos, J. V.; Morcillo, G. Mixed Silver/Gold Colloids: A Study of Their Formation, Morphology, and Surface-Enhanced Raman Activity. *Langmuir* **2000**, *16* (25), 9722–9728. <https://doi.org/10.1021/la000557s>.

- (30) Die Forschung Belegt: Heilwasser Wirkt.
- (31) T. Hrstka, J. Dubessy, J. Zacharias,. European Current Research on Fluid Inclusions ECROFI-XXI Abstracts, Montanuniversitaet Leoben, Berichte Der Geologischen Bundesanstalt; Leoben, Austria, 2011.
- (32) Somekawa, T.; Fujita, M. Raman Spectroscopic Measurements of CO_2 Dissolved in Seawater for Laser Remote Sensing in Water. *EPJ Web of Conferences* **2016**, *119*, 25017. <https://doi.org/10.1051/epjconf/201611925017>.
- (33) S. Cinta Pinzaru, M. Ardeleanu, M. M. Venter, Book of Abstract of The 16th. “Prospects for the 3rd Millennium Agriculture”,; Cluj Napoca, 2017.
- (34) Die Mineralquellen Im Unterengadin.
- (35) Halstensen, M.; Jilvero, H.; Jinadasa, W. N.; Jens, K.-J. Equilibrium Measurements of the NH_3 - CO_2 - H_2O System: Speciation Based on Raman Spectroscopy and Multivariate Modeling. *Journal of Chemistry* **2017**, *2017*, 1–13. <https://doi.org/10.1155/2017/7590506>.
- (36) Reimann, B. E. F.; Lewin, J. C.; Volcani, B. E. STUDIES ON THE BIOCHEMISTRY AND FINE STRUCTURE OF SILICA SHELL FORMATION IN DIATOMS. *Journal of Cell Biology* **1965**, *24* (1), 39–55. <https://doi.org/10.1083/jcb.24.1.39>.
- (37) Demirel, Z.; Imamoglu, E.; Conk Dalay, M. Fatty Acid Profile and Lipid Content of *Cylindrotheca Closterium* Cultivated in Air-Lift Photobioreactor: Fatty Acid Profile and Lipid Content. *J. Chem. Technol. Biotechnol.* **2015**, *90* (12), 2290–2296. <https://doi.org/10.1002/jctb.4687>.
- (38) Liang, Y.; Mai, K.; Sun, S. Differences in Growth, Total Lipid Content and Fatty Acid Composition among 60 Clones of *Cylindrotheca Fusiformis*. *J Appl Phycol* **2005**, *17* (1), 61–65. <https://doi.org/10.1007/s10811-005-5525-4>.
- (39) Hildebrand, M.; Doktycz, M. J.; Allison, D. P. Application of AFM in Understanding Biomineral Formation in Diatoms. *Pflugers Arch - Eur J Physiol* **2008**, *456* (1), 127–137. <https://doi.org/10.1007/s00424-007-0388-y>.
- (40) Pletikapić, G.; Žutić, V.; Vinković Vrček, I.; Svetličić, V. Atomic Force Microscopy Characterization of Silver Nanoparticles Interactions with Marine Diatom Cells and Extracellular Polymeric Substance: AFM CHARACTERIZATION OF Ag NPs INTERACTIONS WITH MARINE DIATOMS. *J. Mol. Recognit.* **2012**, *25* (5), 309–317. <https://doi.org/10.1002/jmr.2177>.
- (41) Svetličić, V.; Žutić, V.; Pletikapić, G.; Radić, T. Marine Polysaccharide Networks and Diatoms at the Nanometric Scale. *IJMS* **2013**, *14* (10), 20064–20078. <https://doi.org/10.3390/ijms141020064>.
- (42) Tomar, V. Raman Spectroscopy of Algae: A Review. *J Nanomed Nanotechnol* **2012**, *03* (02). <https://doi.org/10.4172/2157-7439.1000131>.
- (43) Huang, Y. Y.; Beal, C. M.; Cai, W. W.; Ruoff, R. S.; Terentjev, E. M. Micro-Raman Spectroscopy of Algae: Composition Analysis and Fluorescence Background Behavior. *Biotechnol. Bioeng.* **2009**, n/a-n/a. <https://doi.org/10.1002/bit.22617>.
- (44) Jehlička, J.; Edwards, H. G. M.; Oren, A. Raman Spectroscopy of Microbial Pigments. *Appl. Environ. Microbiol.* **2014**, *80* (11), 3286–3295. <https://doi.org/10.1128/AEM.00699-14>.
- (45) Pořízka, P.; Prochazková, P.; Prochazka, D.; Sládková, L.; Novotný, J.; Petrilak, M.; Brada, M.; Samek, O.; Pilát, Z.; Zemánek, P.; Adam, V.; Kizek, R.; Novotný, K.; Kaiser, J. Algal Biomass Analysis by Laser-Based Analytical Techniques—A Review. *Sensors* **2014**, *14* (9), 17725–17752. <https://doi.org/10.3390/s140917725>.

- (46) Premvardhan, L.; Bordes, L.; Beer, A.; Büchel, C.; Robert, B. Carotenoid Structures and Environments in Trimeric and Oligomeric Fucoxanthin Chlorophyll *a/c*₂ Proteins from Resonance Raman Spectroscopy. *J. Phys. Chem. B* **2009**, *113* (37), 12565–12574. <https://doi.org/10.1021/jp903029g>.
- (47) Stauber, J. L.; Jeffrey, S. W. PHOTOSYNTHETIC PIGMENTS IN FIFTY-ONE SPECIES OF MARINE DIATOMS. *J. Phycol* **1988**, *24* (2), 158–172. <https://doi.org/10.1111/j.1529-8817.1988.tb04230.x>.
- (48) Kuczynska, P.; Jemiola-Rzeminska, M.; Strzalka, K. Photosynthetic Pigments in Diatoms. *Marine Drugs* **2015**, *13* (9), 5847–5881. <https://doi.org/10.3390/md13095847>.
- (49) Grosser, K.; Zedler, L.; Schmitt, M.; Dietzek, B.; Popp, J.; Pohnert, G. Disruption-Free Imaging by Raman Spectroscopy Reveals a Chemical Sphere with Antifouling Metabolites around Macroalgae. *Biofouling* **2012**, *28* (7), 687–696. <https://doi.org/10.1080/08927014.2012.700306>.
- (50) Pinzaru, S. C.; Müller, C.; Tomšić, S.; Venter, M. M.; Brezestean, I.; Ljubimir, S.; Glamuzina, B. Live Diatoms Facing Ag Nanoparticles: Surface Enhanced Raman Scattering of Bulk *Cylindrotheca closterium* Pennate Diatoms and of the Single Cells. *RSC Adv.* **2016**, *6* (49), 42899–42910. <https://doi.org/10.1039/C6RA04255D>.
- (51) Sumper, M.; Kröger, N. Silica Formation in Diatoms: The Function of Long-Chain Polyamines and Silaffins. *J. Mater. Chem.* **2004**, *14* (14), 2059–2065. <https://doi.org/10.1039/B401028K>.
- (52) Pinzaru, S. C.; Pavel, I. E. SERS and Pharmaceuticals. In *Surface Enhanced Raman Spectroscopy*; Schlücker, S., Ed.; Wiley-VCH Verlag GmbH & Co. KGaA: Weinheim, Germany, 2010; pp 129–154. <https://doi.org/10.1002/9783527632756.ch6>.
- (53) Pinzaru, S. C. P., C. Müller, S. Tomšić, I. Ujević, A. Bratoš; Cetinić, B. I. Cozar, R. Stiufo, M. M. Venter and; B. Glamuzina. Noble Metal Nanoparticles in Seawater: Nano Risk Towards Aquatic Organisms Assessed by SERS. In *Proc. ICAVS 8*, ed. B. Lendl, C. Koch, M. Kra, J. Ofner and G. Ramer, Vienna; Viena 2015; pp 106–107.
- (54) Najdek, M.; Blažina, M.; Djakovac, T.; Kraus, R. The Role of the Diatom *Cylindrotheca closterium* in a Mucilage Event in the Northern Adriatic Sea: Coupling with High Salinity Water Intrusions. *Journal of Plankton Research* **2005**, *27* (9), 851–862. <https://doi.org/10.1093/plankt/fbi057>.
- (55) Suman, K.; Kiran, T.; Devi, U. K.; Sarma, N. S. Culture Medium Optimization and Lipid Profiling of *Cylindrotheca*, a Lipid- and Polyunsaturated Fatty Acid-Rich Pennate Diatom and Potential Source of Eicosapentaenoic Acid. *Botanica Marina* **2012**, *55* (3). <https://doi.org/10.1515/bot-2011-0076>.
- (56) Müller, C.; Glamuzina, B.; Pozniak, I.; Weber, K.; Cialla, D.; Popp, J.; Cîntă Pinzaru, S. Amnesic Shellfish Poisoning Biotxin Detection in Seawater Using Pure or Amino-Functionalized Ag Nanoparticles and SERS. *Talanta* **2014**, *130*, 108–115. <https://doi.org/10.1016/j.talanta.2014.06.059>.
- (57) Schie, I. W.; Nolte, L.; Pedersen, T. L.; Smith, Z.; Wu, J.; Yahiatène, I.; Newman, J. W.; Huser, T. Direct Comparison of Fatty Acid Ratios in Single Cellular Lipid Droplets as Determined by Comparative Raman Spectroscopy and Gas Chromatography. *Analyst* **2013**, *138* (21), 6662. <https://doi.org/10.1039/c3an00970j>.
- (58) Meksiarun, P.; Spegazzini, N.; Matsui, H.; Nakajima, K.; Matsuda, Y.; Sato, H. In Vivo Study of Lipid Accumulation in the Microalgae Marine Diatom *Thalassiosira pseudonana* Using Raman Spectroscopy. *Appl Spectrosc* **2015**, *69* (1), 45–51. <https://doi.org/10.1366/14-07598>.
- (59) Samek, O.; Zemánek, P.; Jonáš, A.; Telle, H. H. Characterization of Oil-Producing Microalgae Using Raman Spectroscopy. *Laser Phys. Lett.* **2011**, *8* (10), 701–709. <https://doi.org/10.1002/lapl.201110060>.

- (60) Pennington, F.; Guillard, R. R. L.; Liaaen-Jensen, S. Carotenoid Distribution Patterns in Bacillariophyceae (Diatoms). *Biochemical Systematics and Ecology* **1988**, *16* (7–8), 589–592. [https://doi.org/10.1016/0305-1978\(88\)90067-1](https://doi.org/10.1016/0305-1978(88)90067-1).
- (61) Kuczynska, P.; Jemiola-Rzeminska, M. Isolation and Purification of All-Trans Diadinoxanthin and All-Trans Diatoxanthin from Diatom *Phaeodactylum Tricornutum*. *J Appl Phycol* **2017**, *29* (1), 79–87. <https://doi.org/10.1007/s10811-016-0961-x>.
- (62) Ahel, M., i Terzić, S. Pigment Signatures of Phytoplankton Dynamics in the Northern Adriatic'. *Chemica Acta*, *71*(2), str. 199-215. *Preuzeto s* **1998**.
- (63) Vesna Flander-Putrlje. Examples of High Performance Liquid Chromatography (HPLC) Application in Marine Ecology Studies in the Northern Adriatic. *NATURA SLOVENIAE* **2009**, 5–23.
- (64) Leruste, A.; Hatey, E.; Bec, B.; De Wit, R. Selecting an HPLC Method for Chemotaxonomic Analysis of Phytoplankton Community in Mediterranean Coastal Lagoons, 2015. <https://doi.org/10.1285/I1825229XV9N1P20>.
- (65) Cates, N.; Einck, V. J.; Micklow, L.; Morère, J.; Okoroanyanwu, U.; Watkins, J. J.; Furst, S. Roll-to-Roll Nanoimprint Lithography Using a Seamless Cylindrical Mold Nanopatterned with a High-Speed Mastering Process. *Nanotechnology* **2021**, *32* (15), 155301. <https://doi.org/10.1088/1361-6528/abd9f1>.
- (66) Zhang, C.; Yi, P.; Peng, L.; Lai, X.; Chen, J.; Huang, M.; Ni, J. Continuous Fabrication of Nanostructure Arrays for Flexible Surface Enhanced Raman Scattering Substrate. *Sci Rep* **2017**, *7* (1), 39814. <https://doi.org/10.1038/srep39814>.
- (67) Liu, S.; Xu, Z.; Sun, T.; Zhao, W.; Wu, X.; Ma, Z.; Xu, H.; He, J.; Chen, C. Large-Scale Fabrication of Polymer/Ag Core–Shell Nanorod Array as Flexible SERS Substrate by Combining Direct Nanoimprint and Electroless Deposition. *Appl. Phys. A* **2014**, *115* (3), 979–984. <https://doi.org/10.1007/s00339-013-7917-7>.
- (68) Zhang, R.; Lai, Y.; Zhan, J. Enhancing the Activity of Silver Nanowire Membranes by Electrochemical Cyclic Voltammetry as Highly Sensitive Flexible SERS Substrate for On-Site Analysis. *Nanomaterials* **2021**, *11* (3), 672. <https://doi.org/10.3390/nano11030672>.
- (69) Lee, T.; Jung, S.; Kwon, S.; Kim, W.; Park, J.; Lim, H.; Lee, J. Formation of Interstitial Hot-Spots Using the Reduced Gap-Size between Plasmonic Microbeads Pattern for Surface-Enhanced Raman Scattering Analysis. *Sensors* **2019**, *19* (5), 1046. <https://doi.org/10.3390/s19051046>.
- (70) Zhang, M.; Jin, C.; Nie, Y.; Ren, Y.; Hao, N.; Xu, Z.; Dong, L.; Zhang, J. X. J. Silver Nanoparticle on Zinc Oxide Array for Label-Free Detection of Opioids through Surface-Enhanced Raman Spectroscopy. *RSC Adv.* **2021**, *11* (19), 11329–11337. <https://doi.org/10.1039/D1RA00760B>.
- (71) Kneipp, K.; Wang, Y.; Kneipp, H.; Perelman, L. T.; Itzkan, I.; Dasari, R. R.; Feld, M. S. Single Molecule Detection Using Surface-Enhanced Raman Scattering (SERS). *Phys. Rev. Lett.* **1997**, *78* (9), 1667–1670. <https://doi.org/10.1103/PhysRevLett.78.1667>.
- (72) Kleinman, S. L.; Ringe, E.; Valley, N.; Wustholz, K. L.; Phillips, E.; Scheidt, K. A.; Schatz, G. C.; Van Duyne, R. P. Single-Molecule Surface-Enhanced Raman Spectroscopy of Crystal Violet Isotopologues: Theory and Experiment. *J. Am. Chem. Soc.* **2011**, *133* (11), 4115–4122. <https://doi.org/10.1021/ja110964d>.
- (73) Liu, B.; Jiang, W.; Wang, H.; Yang, X.; Zhang, S.; Yuan, Y.; Wu, T.; Du, Y. A Surface Enhanced Raman Scattering (SERS) Microdroplet Detector for Trace Levels of Crystal Violet. *Microchim Acta* **2013**, *180* (11–12), 997–1004. <https://doi.org/10.1007/s00604-013-1026-3>.

- (74) Colniță, A.; Marconi, D.; Dina, N. E.; Brezeștean, I.; Bogdan, D.; Turcu, I. 3D Silver Metallized Nanotrenches Fabricated by Nanoimprint Lithography as Flexible SERS Detection Platform. *Spectrochimica Acta Part A: Molecular and Biomolecular Spectroscopy* **2022**, *276*, 121232. <https://doi.org/10.1016/j.saa.2022.121232>.
- (75) Farcau, C.; Marconi, D.; Colniță, A.; Brezeștean, I.; Barbu-Tudoran, L. Gold Nanopost-Shell Arrays Fabricated by Nanoimprint Lithography as a Flexible Plasmonic Sensing Platform. *Nanomaterials* **2019**, *9* (11), 1519. <https://doi.org/10.3390/nano9111519>.
- (76) Pimentel, A.; Araújo, A.; Coelho, B.; Nunes, D.; Oliveira, M.; Mendes, M.; Águas, H.; Martins, R.; Fortunato, E. 3D ZnO/Ag Surface-Enhanced Raman Scattering on Disposable and Flexible Cardboard Platforms. *Materials* **2017**, *10* (12), 1351. <https://doi.org/10.3390/ma10121351>.
- (77) Ramohlola, K. E.; Iwuoha, E. I.; Hato, M. J.; Modibane, K. D. Instrumental Techniques for Characterization of Molybdenum Disulphide Nanostructures. *Journal of Analytical Methods in Chemistry* **2020**, *2020*, 1–29. <https://doi.org/10.1155/2020/8896698>.
- (78) Rasmussen, B.; Fletcher, I. R.; Brocks, J. J.; Kilburn, M. R. Reassessing the First Appearance of Eukaryotes and Cyanobacteria. *Nature* **2008**, *455* (7216), 1101–1104. <https://doi.org/10.1038/nature07381>.
- (79) Paerl, H. W.; Fulton, R. S.; Moisaner, P. H.; Dyble, J. Harmful Freshwater Algal Blooms, With an Emphasis on Cyanobacteria. *The Scientific World JOURNAL* **2001**, *1*, 76–113. <https://doi.org/10.1100/tsw.2001.16>.
- (80) Huisman, J.; Codd, G. A.; Paerl, H. W.; Ibelings, B. W.; Verspagen, J. M. H.; Visser, P. M. Cyanobacterial Blooms. *Nat Rev Microbiol* **2018**, *16* (8), 471–483. <https://doi.org/10.1038/s41579-018-0040-1>.
- (81) Merel, S.; Walker, D.; Chicana, R.; Snyder, S.; Baurès, E.; Thomas, O. State of Knowledge and Concerns on Cyanobacterial Blooms and Cyanotoxins. *Environment International* **2013**, *59*, 303–327. <https://doi.org/10.1016/j.envint.2013.06.013>.
- (82) Cazenave, J.; Wunderlin, D. A.; Bistoni, M. de los Á.; Amé, M. V.; Krause, E.; Pflugmacher, S.; Wiegand, C. Uptake, Tissue Distribution and Accumulation of Microcystin-RR in *Corydoras Paleatus*, *Jenynsia Multidentata* and *Odontesthes Bonariensis*. *Aquatic Toxicology* **2005**, *75* (2), 178–190. <https://doi.org/10.1016/j.aquatox.2005.08.002>.
- (83) Carmichael, W. W. Health Effects of Toxin-Producing Cyanobacteria: “The CyanoHABs.” *Human and Ecological Risk Assessment: An International Journal* **2001**, *7* (5), 1393–1407. <https://doi.org/10.1080/20018091095087>.
- (84) Romanis, C. S.; Pearson, L. A.; Neilan, B. A. Cyanobacterial Blooms in Wastewater Treatment Facilities: Significance and Emerging Monitoring Strategies. *Journal of Microbiological Methods* **2021**, *180*, 106123. <https://doi.org/10.1016/j.mimet.2020.106123>.
- (85) Munoz, M.; Cirés, S.; de Pedro, Z. M.; Colina, J. Á.; Velásquez-Figueroa, Y.; Carmona-Jiménez, J.; Caro-Borrero, A.; Salazar, A.; Santa María Fuster, M.-C.; Contreras, D.; Perona, E.; Quesada, A.; Casas, J. A. Overview of Toxic Cyanobacteria and Cyanotoxins in Ibero-American Freshwaters: Challenges for Risk Management and Opportunities for Removal by Advanced Technologies. *Science of The Total Environment* **2021**, *761*, 143197. <https://doi.org/10.1016/j.scitotenv.2020.143197>.
- (86) Duy, T. N.; Lam, P. K. S.; Shaw, G. R.; Connell, D. W. Toxicology and Risk Assessment of Freshwater Cyanobacterial (Blue-Green Algal) Toxins in Water. In *Reviews of Environmental Contamination and Toxicology*; Ware, G. W., Ed.; Reviews of Environmental Contamination and Toxicology; Springer New York: New York, NY, 2000; Vol. 163, pp 113–185. https://doi.org/10.1007/978-1-4757-6429-1_3.
- (87) Dietrich, D.; Hoeger, S. Guidance Values for Microcystins in Water and Cyanobacterial Supplement Products (Blue-Green Algal Supplements): A Reasonable or Misguided Approach?

- Toxicology and Applied Pharmacology* **2005**, *203* (3), 273–289. <https://doi.org/10.1016/j.taap.2004.09.005>.
- (88) Lage, S.; Mazur-Marzec, H.; Gorokhova, E. Competitive Interactions as a Mechanism for Chemical Diversity Maintenance in Nodularia Spumigena. *Sci Rep* **2021**, *11* (1), 8970. <https://doi.org/10.1038/s41598-021-88361-x>.
- (89) Gehringer, M. M.; Adler, L.; Roberts, A. A.; Moffitt, M. C.; Mihali, T. K.; Mills, T. J. T.; Fieker, C.; Neilan, B. A. Nodularin, a Cyanobacterial Toxin, Is Synthesized in Planta by Symbiotic Nostoc Sp. *ISME J* **2012**, *6* (10), 1834–1847. <https://doi.org/10.1038/ismej.2012.25>.
- (90) Moffitt, M. C.; Blackburn, S. I.; Neilan, B. A. RRNA Sequences Reflect the Ecophysiology and Define the Toxic Cyanobacteria of the Genus Nodularia. *International Journal of Systematic and Evolutionary Microbiology* **2001**, *51* (2), 505–512. <https://doi.org/10.1099/00207713-51-2-505>.
- (91) Beattie, K. A.; Kaya, K.; Codd, G. A. The Cyanobacterium Nodularia PCC 7804, of Freshwater Origin, Produces [L-Har2]Nodularin. *Phytochemistry* **2000**, *54* (1), 57–61. [https://doi.org/10.1016/S0031-9422\(00\)00045-5](https://doi.org/10.1016/S0031-9422(00)00045-5).
- (92) Dittmann, E.; Wiegand, C. Cyanobacterial Toxins - Occurrence, Biosynthesis and Impact on Human Affairs. *Mol. Nutr. Food Res.* **2006**, *50* (1), 7–17. <https://doi.org/10.1002/mnfr.200500162>.
- (93) Jokela, J.; Heinilä, L. M. P.; Shishido, T. K.; Wahlsten, M.; Fewer, D. P.; Fiore, M. F.; Wang, H.; Haapaniemi, E.; Permi, P.; Sivonen, K. Production of High Amounts of Hepatotoxin Nodularin and New Protease Inhibitors Pseudospumigins by the Brazilian Benthic Nostoc Sp. CENA543. *Front. Microbiol.* **2017**, *8*, 1963. <https://doi.org/10.3389/fmicb.2017.01963>.
- (94) Meissner, S.; Fastner, J.; Dittmann, E. Microcystin Production Revisited: Conjugate Formation Makes a Major Contribution: Production of Cyanobacterial Toxins Strongly Underestimated. *Environ Microbiol* **2013**, *15* (6), 1810–1820. <https://doi.org/10.1111/1462-2920.12072>.
- (95) Massey, I. Y.; Wu, P.; Wei, J.; Luo, J.; Ding, P.; Wei, H.; Yang, F. A Mini-Review on Detection Methods of Microcystins. *Toxins* **2020**, *12* (10), 641. <https://doi.org/10.3390/toxins12100641>.
- (96) Forastier, M. E.; Zalocar, Y.; Andrinolo, D.; Domitrovic, H. A. Occurrence and Toxicity of Microcystis Aeruginosa (Cyanobacteria) in the Paraná River, Downstream of the Yacretá Dam (Argentina). *Rev Biol Trop* **2016**, *64* (1), 203–211.
- (97) Vasconcelos, V. M.; Sivonen, K.; Evans, W. R.; Carmichael, W. W.; Namikoshi, M. Hepatotoxic Microcystin Diversity in Cyanobacterial Blooms Collected in Portuguese Freshwaters. *Water Research* **1996**, *30* (10), 2377–2384. [https://doi.org/10.1016/0043-1354\(96\)00152-2](https://doi.org/10.1016/0043-1354(96)00152-2).
- (98) Li, M.; Paidi, S. K.; Sakowski, E.; Preheim, S.; Barman, I. Ultrasensitive Detection of Hepatotoxic Microcystin Production from Cyanobacteria Using Surface-Enhanced Raman Scattering Immunosensor. *ACS Sens.* **2019**, *4* (5), 1203–1210. <https://doi.org/10.1021/acssensors.8b01453>.
- (99) Li, M.; Lin, H.; Paidi, S. K.; Mesyngier, N.; Preheim, S.; Barman, I. A Fluorescence and Surface-Enhanced Raman Spectroscopic Dual-Modal Aptasensor for Sensitive Detection of Cyanotoxins. *ACS Sens.* **2020**, *5* (5), 1419–1426. <https://doi.org/10.1021/acssensors.0c00307>.
- (100) Halvorson, R. A.; Vikesland, P. J. Drop Coating Deposition Raman (DCDR) for Microcystin-LR Identification and Quantitation. *Environ. Sci. Technol.* **2011**, *45* (13), 5644–5651. <https://doi.org/10.1021/es200255y>.
- (101) Kočíšová, E.; Sayedová, S.; Procházka, M. Drop Coating Deposition Raman Scattering of Selected Small Molecules of Biological Importance. *J Raman Spectrosc* **2020**, *51* (5), 871–874. <https://doi.org/10.1002/jrs.5840>.

- (102) Kuižová, A.; Příkryl, M.; Procházka, M.; Kočišová, E. Drop Coating Deposition Raman (DCDR) Spectroscopy of Contaminants. *Spectrochimica Acta Part A: Molecular and Biomolecular Spectroscopy* **2021**, *262*, 120109. <https://doi.org/10.1016/j.saa.2021.120109>.
- (103) Kočišová, E.; Procházka, M.; Vaculčíaková, L. Drop-Coating Deposition Raman (DCDR) Spectroscopy as a Tool for Membrane Interaction Studies: Liposome–Porphyrin Complex. *Appl Spectrosc* **2015**, *69* (8), 939–945. <https://doi.org/10.1366/14-07836>.
- (104) Tahir, M. A.; Zhang, X.; Cheng, H.; Xu, D.; Feng, Y.; Sui, G.; Fu, H.; Valev, V. K.; Zhang, L.; Chen, J. Klarite as a Label-Free SERS-Based Assay: A Promising Approach for Atmospheric Bioaerosol Detection. *Analyst* **2020**, *145* (1), 277–285. <https://doi.org/10.1039/C9AN01715A>.
- (105) *EU Policy for a Sustainable Use of Pesticide: The Story behind the Strategy*; Europäische Kommission, Ed.; Environment; Office for Official Publications of the European Commission: Luxembourg, 2007.
- (106) Chamuah, N.; Bhuyan, N.; Das, P. P.; Ojah, N.; Choudhary, A. J.; Medhi, T.; Nath, P. Gold-Coated Electrospun PVA Nanofibers as SERS Substrate for Detection of Pesticides. *Sensors and Actuators B: Chemical* **2018**, *273*, 710–717. <https://doi.org/10.1016/j.snb.2018.06.079>.
- (107) Zhou, H.; Li, X.; Wang, L.; Liang, Y.; Jialading, A.; Wang, Z.; Zhang, J. Application of SERS Quantitative Analysis Method in Food Safety Detection. *Reviews in Analytical Chemistry* **2021**, *40* (1), 173–186. <https://doi.org/10.1515/revac-2021-0132>.
- (108) Fu, G.; Sun, D.-W.; Pu, H.; Wei, Q. Fabrication of Gold Nanorods for SERS Detection of Thiabendazole in Apple. *Talanta* **2019**, *195*, 841–849. <https://doi.org/10.1016/j.talanta.2018.11.114>.
- (109) Müller, C.; David, L.; Chiş, V.; Pînzaru, S. C. Detection of Thiabendazole Applied on Citrus Fruits and Bananas Using Surface Enhanced Raman Scattering. *Food Chemistry* **2014**, *145*, 814–820. <https://doi.org/10.1016/j.foodchem.2013.08.136>.
- (110) Oliveira, M. J. S.; Rubira, R. J. G.; Furini, L. N.; Batagin-Neto, A.; Constantino, C. J. L. Detection of Thiabendazole Fungicide/Parasiticide by SERS: Quantitative Analysis and Adsorption Mechanism. *Applied Surface Science* **2020**, *517*, 145786. <https://doi.org/10.1016/j.apsusc.2020.145786>.
- (111) Maier-Bode, H. Properties, Effect, Residues and Analytics of the Insecticide Endosulfan. In *Residue Reviews / Rückstands-Berichte*; Gunther, F. A., Ed.; Reviews of Environmental Contamination and Toxicology; Springer US: New York, NY, 1968; Vol. 22, pp 1–44. https://doi.org/10.1007/978-1-4615-8434-6_1.
- (112) Schmidt, W. F.; Hapeman, C. J.; McConnell, L. L.; Mookherji, S.; Rice, C. P.; Nguyen, J. K.; Qin, J.; Lee, H.; Chao, K.; Kim, M. S. Temperature-Dependent Raman Spectroscopic Evidence of and Molecular Mechanism for Irreversible Isomerization of β -Endosulfan to α -Endosulfan. *J. Agric. Food Chem.* **2014**, *62* (9), 2023–2030. <https://doi.org/10.1021/jf404404w>.
- (113) United Nations Targets Widely-Used Pesticide Endosulfan for Phase Out; United Nations Environment Programme: Geneva, 2011.
- (114) Weber, J.; Halsall, C. J.; Muir, D.; Teixeira, C.; Small, J.; Solomon, K.; Hermanson, M.; Hung, H.; Bidleman, T. Endosulfan, a Global Pesticide: A Review of Its Fate in the Environment and Occurrence in the Arctic. *Science of The Total Environment* **2010**, *408* (15), 2966–2984. <https://doi.org/10.1016/j.scitotenv.2009.10.077>.
- (115) Becker, L.; Scheringer, M.; Schenker, U.; Hungerbühler, K. Assessment of the Environmental Persistence and Long-Range Transport of Endosulfan. *Environmental Pollution* **2011**, *159* (6), 1737–1743. <https://doi.org/10.1016/j.envpol.2011.02.012>.
- (116) Guerrini, L.; Aliaga, A. E.; Cárcamo, J.; Gómez-Jeria, J. S.; Sanchez-Cortes, S.; Campos-Valette, M. M.; García-Ramos, J. V. Functionalization of Ag Nanoparticles with the Bis-

- Acridinium Lucigenin as a Chemical Assembler in the Detection of Persistent Organic Pollutants by Surface-Enhanced Raman Scattering. *Analytica Chimica Acta* **2008**, *624* (2), 286–293. <https://doi.org/10.1016/j.aca.2008.06.038>.
- (117) Lee, P. C.; Meisel, D. Adsorption and Surface-Enhanced Raman of Dyes on Silver and Gold Sols. *J. Phys. Chem.* **1982**, *86* (17), 3391–3395. <https://doi.org/10.1021/j100214a025>.
- (118) Kim, Min Kyung; Lee, Chul-Jae; Jung, Young Mee; Lee, Mu-Sang. Surface-Enhanced Raman Spectroscopy of Benzimidazolic Fungicides: Benzimidazole and Thiabendazole. *Bulletin of the Korean Chemical Society* **2009**, *30* (12), 2930–2934. <https://doi.org/10.5012/BKCS.2009.30.12.2930>.
- (119) Moldovan, R.; Iacob, B.-C.; Farcău, C.; Bodoki, E.; Oprean, R. Strategies for SERS Detection of Organochlorine Pesticides. *Nanomaterials* **2021**, *11* (2), 304. <https://doi.org/10.3390/nano11020304>.
- (120) Kubackova, J.; Izquierdo-Lorenzo, I.; Jancura, D.; Miskovsky, P.; Sanchez-Cortes, S. Adsorption of Linear Aliphatic α,ω -Dithiols on Plasmonic Metal Nanoparticles: A Structural Study Based on Surface-Enhanced Raman Spectra. *Phys. Chem. Chem. Phys.* **2014**, *16* (23), 11461–11470. <https://doi.org/10.1039/C4CP00424H>.
- (121) Jiang, X.; Lai, Y.; Wang, W.; Jiang, W.; Zhan, J. Surface-Enhanced Raman Spectroscopy Detection of Polybrominated Diphenylethers Using a Portable Raman Spectrometer. *Talanta* **2013**, *116*, 14–17. <https://doi.org/10.1016/j.talanta.2013.04.056>.
- (122) Kennedy, B. J.; Spaeth, S.; Dickey, M.; Carron, K. T. Determination of the Distance Dependence and Experimental Effects for Modified SERS Substrates Based on Self-Assembled Monolayers Formed Using Alkanethiols. *J. Phys. Chem. B* **1999**, *103* (18), 3640–3646. <https://doi.org/10.1021/jp984454i>.
- (123) Joo, T. H.; Kim, K.; Kim, M. S. Surface-Enhanced Raman Scattering (SERS) of 1-Propanethiol in Silver Sol. *J. Phys. Chem.* **1986**, *90* (22), 5816–5819. <https://doi.org/10.1021/j100280a069>.
- (124) John Wiley & Sons, Inc. SpectraBase; SpectraBase Compound ID=JyVYUwLwX SpectraBase Spectrum ID=DZu8UBUhp0.
- (125) Bain, C. D.; Troughton, E. B.; Tao, Y. T.; Evall, J.; Whitesides, G. M.; Nuzzo, R. G. Formation of Monolayer Films by the Spontaneous Assembly of Organic Thiols from Solution onto Gold. *J. Am. Chem. Soc.* **1989**, *111* (1), 321–335. <https://doi.org/10.1021/ja00183a049>.
- (126) Schmidt, W. F.; Hapeman, C. J.; Fettinger, J. C.; Rice, C. P.; Bilbouljian, S. Structure and Asymmetry in the Isomeric Conversion of β - to α -Endosulfan. *J. Agric. Food Chem.* **1997**, *45* (4), 1023–1026. <https://doi.org/10.1021/jf970020t>.
- (127) Hassanain, W. A.; Izake, E. L.; Schmidt, M. S.; Ayoko, G. A. Gold Nanomaterials for the Selective Capturing and SERS Diagnosis of Toxins in Aqueous and Biological Fluids. *Biosensors and Bioelectronics* **2017**, *91*, 664–672. <https://doi.org/10.1016/j.bios.2017.01.032>.

Appendix 1. Results and dissemination

Published articles on the Thesis subject

1. **Ioana Brezeştean**, Maricel Bocăneală, Ana Maria Raluca Gherman, Sebastian Alin Porav, Irina Kacsó, Elena Rakosy-Tican, Nicoleta Elena Dina, *Spectroscopic investigation of exopolysaccharides purified from *Arthrospira plantensis* cultures as potential bioresources*, Journal of Molecular Structure, Volume 1246, 2021, ISSN 0022-2860, <https://doi.org/10.1016/j.molstruc.2021.131228>. IF: 3.196 AIS: 0.293
2. Simona Cîntă Pînzaru, Mircea Ardeleanu, **Ioana Brezeştean**, Fran Nekvapil, Monica M. Venţer, *Biogeochemical specificity of natural carbonated spring waters from Swiss Alps revealed by surface enhanced Raman scattering and Raman spectroscopy tools*, Analytical Methods, Issue 6, 2019, <https://doi.org/10.1039/C8AY02580K>. IF: 2.73 AIS: 0.415
3. Simona Cîntă Pînzaru, Csilla Muller, Sanja Tomsic, Monica M. Venţer, **Ioana Brezeştean**, Stijepo Ljubimird, Branko Glamuzina *Live diatoms facing Ag nanoparticles: surface enhanced Raman scattering of bulk *Cylindrotheca closterium* pennate diatoms and of the single cells*, RSC Advances, 2016, 6, 42899, doi.org/10.1039/C6RA04255D IF: 3.108 AIS: 0.589
4. Fran Nekvapil, **Ioana Brezeştean**, Geza Lazăr, Călin Fîrţa, Simona Cîntă Pînzaru, *Resonance Raman and SERRS of fucoxanthin: Prospects for carotenoid quantification in live diatom cells*, Journal of Molecular Structure, Volume 1250, Part 1, 2022, 131608, <https://doi.org/10.1016/j.molstruc.2021.131608> IF: 3.196 AIS: 0.293
5. Alia Colniţă, Daniel Marconi, Nicoleta Elena Dina, **Ioana Brezeştean**, Diana Bogdan, Ioan Turcu *3D silver metallized nanotrenches fabricated by nanoimprint lithography as flexible SERS detection platform*, Spectrochimica Acta Part A IF: 4.098 AIS: 0.462

Submitted articles on the Thesis subject

1. **Ioana Brezeştean**, Ana Maria Raluca Gherman, Alia Colniţă, Nicoleta Elena Dina, Vasile Chiş, Leontin David, Simona Cîntă-Pînzaru *Detection and characterization of nodularin by using label-free surface-enhanced spectroscopic techniques*, Spectrochimica Acta Part A IF: 4.098 AIS: 0.462- Trimis spre publicare
2. **Ioana Brezeştean**, Nicoleta Toşa, Alexandra Fălămaş, Denisa Cuibus, Cristina M. Muntean, Bogdan Cozar, Camelia Groşan, Attila Bende, Cosmin Farcău, *Silver nanoparticle films obtained by convective self-assembly as a platform for surface-enhanced Raman spectroscopy analyses of pesticides*, Frontiers in Chemistry IF: 5.221 AIS: 1.009- Under review

Other ISI published articles

-
1. Fran Nekvapil, **Ioana Brezeștean**, Simona Cîntă Pînzaru, Vasile Chiș, Daniel Barchewitz, Branko Glamuzina; *Citrus fruits freshness assessment using Raman spectroscopy*; *Food Chemistry*; DOI: 10.1016/j.foodchem.2017.09.105 IF: AIF
 2. Simona Cîntă Pînzaru, Fran Nekvapil, **Ioana Brezeștean**, C. Muller, V. Chiș; *Microsphere packages of carotenoids: intact sea urchin eggs tracked by Raman spectroscopy tools*; DOI:10.1039/C9PP00181
 3. **Ioana Brezeștean**, Simona Cîntă Pînzaru, Alina Tantau, Nicole Har, Monica Vențer; *Analytical study of gallstones in patients from Transylvania, Romania* January 2015 *Studia Universitatis Babeș-Bolyai Chemia* 1(LX 1):29-43.
 4. Cosmin Farcau, Daniel Marconi, Alia Colniță, **Ioana Brezeștean**, Lucian Barbu-Tudoran, *Gold Nanopost-Shell Arrays Fabricated by Nanoimprint Lithography as a Flexible Plasmonic Sensing Platform* *Nanomaterials*, (Basel). 2019 Oct 25;9(11):1519. doi: 10.3390/nano9111519
 5. Alia Colniță, Daniel Marconi, **Ioana Brezeștean**, Roxana-Diana Pașca, Irina Kacso, Lucian Barbu-Tudoran, Ioan Turcu, *High-Throughput Fabrication of Anti-Counterfeiting Nanopillar-Based Quick Response (QR) Codes Using Nanoimprint Lithography*, *Analytical Letters* 54.1-2 (2021): 302-313, doi.org/10.1080/00032719.2020.1769123
 6. Elisabeta Stamate, Octavian Dumitru Pavel, Rodica Zavoianu, **Ioana Brezeștean**, Alexandra Ciorîță, Ruxandra Bîrjega, Katja Neubauer, Angela Köckritz, Ioan-Cezar Marcu, *Ce-Containing MgAl-Layered Double Hydroxide-Graphene Oxide Hybrid Materials as Multifunctional Catalysts for Organic Transformations*, *Materials* 2021, 14(23), 7457; <https://doi.org/10.3390/ma14237457>
 7. Alexandra-Elisabeta Stamate, Rodica Zăvoianu, Octavian Dumitru Pavel, Ruxandra Bîrjega, Andreea Matei, Marius Dumitru, **Ioana Brezeștean**, Mariana Osiac, Ioan-Cezar Marcu, *The influence of the preparation method on the physico-chemical properties and catalytic activities of Ce-modified LDH structures used as catalysts in condensation reactions*, *Molecules* 2021, 26(20), 6191; <https://doi.org/10.3390/molecules26206191>
 8. Adrian Calborean, Alia Colniță, Ioana Grosu, **Ioana Brezeștean**, Roxana-Diana Pașca, Lucian Barbu-Tudoran, Daniel Marconi, *The adhesion of L-methionine amino acid through Dip Pen Nanolithography on silver thin films grown by Molecular Beam Epitaxy technique*, *Journal of Molecular Structure*, Volume 1244, 2021, <https://doi.org/10.1016/j.molstruc.2021.131247>

9. Vlad-Alexandru Toma, Alia Colnita, **Ioana Brezestean**, Bogdan Dume, Ioana Roman, Ioan Turcu, STUDIA UBB CHEMIA, LXVI, 3, 2021 (p. 187-194)
DOI:10.24193/subbchem.2021.3.11
10. Laurențiu Stăncioiu, Ana Maria Raluca Gherman, **Ioana Brezestean**, Nicoleta Elena Dina, *Vibrational spectral analysis of Sorafenib and its molecular docking study compared to other TKIs*, Journal of Molecular Structure, Volume 1248, 2022, ISSN 0022-2860, <https://doi.org/10.1016/j.molstruc.2021.131507>. IF: 3.196 AIS: 0.29

Articles published in BDI journals

1. Niculaescu Carmen, **Ioana Brezestean**, Lung Claudiu, Todica Mihai, *Fluorescence investigation of some polystyrene samples thermally degraded*, Studia Universitatis Babeș-Bolyai, Physica . Dec2018, Vol. 63 Issue 1/2, p19-26. 8p.
2. Simona Cîntă Pînzaru; Csilla Muller, **Ioana Brezestean**, Daniel Barchewits, Branko Glamuzina *Cyanobacteria Detection and Raman Spectroscopy Characterization with a Highly Sensitive, High Resolution Fiber Optic Portable Raman System* STUDIA UBB PHYSICA, Vol. 61 (LXI), 1, 2016;
3. **Brezestean**, S. Cîntă Pînzaru, Fran Nekvapil, Analysis of hypersaline water from Cojocna Balneary Resorts (Romania) using Raman Spectroscopy Tehniques; ; ISSN 2067-743X, pp 3-13;